

This is the author's version (post-print) of the work that was accepted for publication by the Journal of Sound and Vibration in May 2021.
© 2021 – This manuscript version is made available under the CC-BY-NC-ND 4.0 license:
<https://creativecommons.org/licenses/by-nc-nd/4.0/>
The final version was published by the Journal of Sound and Vibration:
<https://doi.org/10.1016/j.jsv.2021.116221>

Comparison of Predicted Fan Broadband Noise Using a Two- versus a Three-Dimensional Synthetic Turbulence Method

Carolin Kissner^{1,*}, Sébastien Guérin²

German Aerospace Center (DLR), Müller-Breslau-Str. 8, 10623 Berlin, Germany

Abstract

Fan broadband noise - in particular broadband rotor-stator-interaction noise - is a significant noise source of modern aircraft. However, its accurate prediction remains a challenge. RANS-informed synthetic turbulence methods are increasingly applied for these types of noise predictions as they present a compromise between accuracy and computational effort. Two-dimensional simulations are especially inexpensive but their results are not necessarily representative for the entire fan stage. To investigate this issue, the authors present the expansion of an approach based on the fast Random Particle Mesh method to three-dimensional space and apply it to the AneCom AeroTest Rotor 1 fan stage. The three-dimensional simulations are compared in detail to two-dimensional simulations to quantify and analyze observed differences between the results. As a consequence, a correction technique for the two-dimensional simulation results is proposed.

Keywords: fan broadband noise; synthetic turbulence; fast random particle mesh; ACAT1 fan; rotor-stator-interaction; mean line prediction

*Corresponding author

Email address: carolin.kissner@dlr.de (Carolin Kissner)

¹Research Engineer, Institute of Propulsion Technology, Department of Engine Acoustics

²Senior Research Scientist, Institute of Propulsion Technology, Department of Engine Acoustics

Nomenclature

B	number of rotor blades
c_0	speed of sound, m/s
5 $E(\mathbf{k})$	energy spectrum of turbulence, m^3/s^2
f	frequency, Hz
${}_2F_1$	Gaussian hypergeometric function
k	turbulent kinetic energy, m^2/s^2
k_i	wavenumber in direction i , $1/\text{m}$
10 k_e	characteristic wavenumber, $1/\text{m}$
\hat{k}_i	wavenumber in direction i normalized by k_e
l_3	spanwise correlation length of turbulence, m
M	free stream Mach number
p	pressure, Pa
15 r	radius, m
r_0	rotor tip radius, m
s	streamline position
s_V	stator pitch, m
S_{22}	upwash velocity frequency spectral density, m^2/s
20 S_{pp}	pressure frequency spectral density, Pa^2/s
u	velocity, m/s
V	number of stator vanes

	β	compressibility factor
	γ	blade sweep angle, rad.
25	ϑ	angle, rad.
	Γ	gamma function
	κ_0	free-field acoustic wavenumber, 1/m
	λ_x	in-duct acoustic wavelength in the axial direction, m
	Λ	integral turbulent length scale, m
30	ρ	density, kg/m ³
	σ_L	source term, Pa
	Φ_{ii}	velocity wavenumber spectrum relative to direction i, m/s ²

Sub- and Superscripts

	'	fluctuating variable
35	0	mean variable
	1	streamwise direction
	2	upwash direction
	2D	two-dimensional
	3	radial direction
40	3D	three-dimensional
	—	radially or circumferentially averaged

1. Introduction

Broadband rotor-stator interaction (RSI) noise in the fan stage of modern engines is a primary sound source of commercial aircraft, particularly during
45 flight phases in close proximity to the ground. This sound mechanism is driven by the turbulence of the rotor wakes interacting with the surface at the leading edges of the downstream positioned stator row.

Due to the successful application of noise abatement measures aimed at reducing tonal noise, the relative importance of broadband noise to the overall
50 aircraft noise has further increased within recent years. The development and improvement of today's fan broadband noise prediction techniques is therefore crucial for gaining a deeper, physical understanding of the involved aerodynamic, turbulent, and acoustic mechanisms, for improving fast and simple methods based on these findings, and for gaining confidence in terms of achievable prediction accuracy. These objectives are ultimately a key in developing quieter
55 aircraft to meet more stringent noise regulation requirements in the future.

Today, applied methods range from numerical, fully scale-resolving methods, which are able to account for the most complex geometries, to analytical methods, which are inherently limited to rather simple geometries. Analytical methods
60 are based on simplifying assumptions and can yield results within a very short time making them ideal for the use in multidisciplinary design processes, e. g. as detailed by Jaron [1]. Fully scale-resolving methods are capable of accurately representing the physics, but their use is still very costly in terms of the preparation of the setup and in terms of the computation time. These insights
65 can in turn be used to improve simpler methods. Synthetic turbulence methods have also gained popularity. They are hybrid, partly scale-resolving methods, where a separate, highly optimized method addresses each part of the physical problem. While some limitations and modeling assumptions remain, the aim is to capture the physics as accurately as possible and to curb the computational
70 cost compared to fully or other partly scale-resolving methods. Synthetic turbulence methods typically work as follows: A Reynolds Averaged Navier Stokes

(RANS) or an Unsteady Reynolds Averaged Navier Stokes (URANS) simulation is needed to provide inputs for flow and turbulence characteristics. The turbulence statistics are used to synthesize turbulence upstream of the stator
75 vanes. Synthetic turbulence is commonly generated by filtering [2, 3], by superposing random Fourier modes [4–6], or by using synthetic eddies [7–9]. The turbulence is then injected into a computational domain, where it is convected and interacts with the stator leading edges to create noise. High-order, optimized schemes implemented in so-called Computational AeroAcoustics (CAA)
80 solvers enable an efficient calculation of the produced acoustic sound field. The sound in the far field can either be directly determined at sensor positions in the computational domain or by applying a Ffowcs-Williams–Hawkings method relying on pressure fluctuation information on the blade surfaces.

Two-dimensional synthetic turbulence methods are convenient due to their
85 comparatively low computation costs, which enable overnight simulations on regular computers. The fast computations enable extensive parameter studies, e. g. to investigate cylostationary effects [10], the relative importance of background versus wake turbulence [11], rotor blockage effects [12], the influence of anisotropic turbulence [13] etc. Nonetheless, one central issue remains: How
90 representative are these findings for a real, fully three-dimensional fan stage? On the one hand, two-dimensional simulations are restricted to one streamline or radial position making it difficult or entirely impossible to capture three-dimensional flow effects, like flow detachments or three-dimensional geometry features like blade lean, blade sweep, or leading edge serrations. It is also ques-
95 tionable if a solution computed at one single radial position is valid for the entire fan stage. To increase the reliability of results, simulations at multiple streamline positions can be combined [11, 12, 14] or a simulation can be set up using a representative streamline and imposing three-dimensional-equivalent (3D-equivalent) turbulence characteristics as proposed by Kissner et al. [14].
100 On the other hand, there are differences in the sound mechanism between two-dimensional and three-dimensional simulations as the third dimension is essential for capturing several important aspects of the physical problem as will

be addressed during the course of this paper. No universal correction method exists. Instead, multiple different approaches are used:

- 105 • Amiet-based [15] correction techniques were proposed by Dieste [16] and Hainaut et al. [17]. Amiet-based corrections are formulated for an observer positioned in the far-field at 90° relative to the midspan of a single blade. The correction accounts for the fact that the far-field sound propagation of a two-dimensional (2D) space is described by $p \propto \sqrt{r}$, whereas 3D simulation captures a realistic behavior of the sound propagation, where 110 $p \propto r$. The formulation also includes the turbulence correlation length in the spanwise direction to account for the fact that the source at the leading edge is only correlated over a distance, which is typically much shorter than the airfoil span. Thereby, the source correlation length and the turbulence correlation length are assumed to be equal. The Dieste 115 correction further contains a correction to account for the differences in 2D and 3D turbulence spectra, while the Hainaut correction neglects this aspect. Gea-Aguilera [13, 18] proposed the use of a so-called pseudo three-dimensional turbulence for 2D simulations, which is essentially a numerical 120 implementation of Hainaut’s correction. Another correction technique, which was initially proposed by Ewert et al. [19], is identical to Hainaut’s formulation for low Mach numbers. While Ewert’s formulation was originally proposed for analyzing trailing edge noise, it can also be applied to leading edge noise as shown e. g. by Polacsek et al. [20]. It should 125 be noted that these Amiet-based methods are generally only applied for low-speed, single airfoil cases.
- A correction formulated by Wohlbrand et al. [10] accounts for the difference in spectral shape of 2D versus 3D transverse turbulent velocity spectra. As previously mentioned, the Dieste correction can be interpreted as 130 inherently containing this correction.
- Another approach, which was applied e. g. by Blázquez and Corral [12], is to discard subcritical turbulent gusts for 2D simulations. In 3D sim-

ulations, only turbulent modes featuring a supersonic trace velocity, i. e. supercritical modes, produce pressure waves capable of propagating. Due to the absence of the radial dimension, 2D simulations cannot reproduce this physical phenomenon. Instead, all turbulent modes generate sound, which causes 2D simulations to overestimate predicted sound levels. The criterion for distinguishing between subcritical and supercritical turbulent gusts was originally proposed by Graham [21], who formulated similarity rules for describing the loading of thin, single airfoils. Later, Glegg [22] showed that the distinction between sub- and supercritical turbulent modes is also applicable for cascades as he formulated an airfoil response for swept blade rows in free field.

Recently, Kissner et al. [23] expanded the fRPM-fan method - a synthetic turbulence method based on the fast Random Particle Mesh (fRPM) method - to three-dimensional space and presented a first working example for a realistic fan configuration. In addition, an optimization of simulation parameters was performed resulting in significant improvements in the computational effort while still ensuring accurate results. In this work, the authors build on these findings and shift the focus from method development to understanding the physics involved in the simulations. The following research questions are addressed:

- Can the newly implemented 3D fRPM-fan method yield realistic fan broadband noise levels for the AneCom AeroTest Rotor 1 (ACAT1) fan?
- Can the experimental trends observed between different operating points be reproduced by 2D and 3D simulations?
- How do the results of 2D and 3D simulations differ in terms of turbulence realization, in-duct sound power and sound pressure levels? Based on this analysis, is it possible to formulate a reasonable correction for 2D simulations?

In order to investigate these questions, the authors set up 3D and 2D fRPM-

fan simulations at two approach operating points on two different working lines for the ACAT1 fan. In addition, the 2D simulation approach is applied for the first time to two operating points featuring much higher rotational speeds. As
165 an analysis of the turbulence characteristics near the stator leading edges reveals that the relative contribution of background turbulence to the overall turbulence levels is small for this fan configuration, cyclostationary effects are neglected for all simulations, which is in agreement with previous findings [10, 11]. The large data set of simulations allows for analyzing experimental and numerical trends
170 and it allows for a detailed comparison of 2D and 3D results. In formulating reasonable corrections for the 2D simulation results, the aim is to ensure that the correction technique is valid for a range of different operating points.

2. Overview of the fRPM-fan method

To distinguish between different simulation techniques using the fRPM method,
175 the authors use the term fRPM-fan method. The fRPM-fan method denotes a hybrid, fRPM-based synthetic turbulence method, which was specifically optimized for fan applications. The concept of the method was introduced by Wohlbrandt [24]. It consists of running – partly sequentially, partly simultaneously - three different simulation techniques: the Computational Fluid Dynamics (CFD) method, the fast Random Particle Mesh (fRPM) method, and the
180 Computational AeroAcoustics (CAA) method.

A CFD solution - RANS or URANS - is necessary to provide mean flow and turbulence characteristics, which are required as inputs for the fRPM and CAA methods. The fRPM method is a fast implementation of the Random
185 Particle Mesh (RPM) method relying on recursive filter implementations on typically Cartesian grids to speed up simulations [25]. The RPM method was originally developed by Ewert [3]. Three-dimensional in-duct applications are challenging for these filter implementations: 1.) The grids are not Cartesian as the cell length in the circumferential direction increases with the radial
190 2.) Mean flow and turbulence characteristics vary with respect to the radial

position. Therefore, a recursive Gaussian filter featuring a spatially anisotropic formulation was applied. This filter, which was proposed by Purser et al. [26], is advantageous as it can handle slowly changing cell sizes and turbulent length scales.

195 For fan applications, the fRPM method does not directly model source terms but synthesizes time-space-dependent turbulence upstream of the stator row. White noise is scaled by a local variance, i.e. a turbulent kinetic energy, and then spatially filtered by a local length scale. Several Gaussian filters of different filter lengths can be superposed in order to realize a target spectrum, e. g. a
200 von Kármán or a Liepmann spectrum [27]. The variance of each filter depends on an analytical weighting function.

The convection of the synthesized turbulence, the sound generation, and the sound propagation are computed by the CAA solver PIANO [28]. In this work, PErturbed Nonconservative Nonlinear Euler Equations (PENNE) as proposed
205 by Long [29] are solved for the 3D simulations, while Linearized Euler Equations (LEE) are solved for the 2D simulations. This difference in equations is not expected to have any significant impact on the predicted fan broadband noise as Kissner et al. [30] have previously shown that linear effects rather than non-linear effects are dominant for a comparable fan. The choice to apply PENNE
210 for the 3D simulations was motivated by stability implications in flow regions, which are not relevant to the noise generation mechanism. When the synthesized vortices interact with the stator wakes or with regions of detached flow on the stator surfaces, hydrodynamic perturbations arise. When applying LEE, these perturbations grow continuously, which can make the simulation unstable. In
215 reality, hydrodynamic fluctuations grow linearly, saturate, and decay with an increasing distance from the source. The PENNE can more realistically capture this effect and thus have a stabilizing impact in the regions near the trailing edge of the stator vanes. For 2D simulations, there were no such issues with instabilities and therefore, the simpler LEE were used. For both 2D and 3D
220 simulations, a fourth order low-dispersion low-dissipation Runge-Kutta scheme [31] was used for time integration and the dispersion-relation-preserving finite

difference scheme by Tam and Webb [32] was used for the spatial discretization. The fluctuating velocity fields synthesized by the fRPM method are coupled into the CAA domain by adding a relaxation term to the impulse equations as proposed by Ewert et al. [33].

RSI broadband noise is generated when the turbulence interacts with the leading edge of a stator vane. The sound is then propagated to sensor positions located at a distance several stator chords away from the stator to determine sound power or sound pressure levels. Note that the method is technically not restricted to the consideration of rotor-stator-interaction noise, which results from the interaction of the wake turbulence with the stator leading edges. In fact, ingested turbulence can be considered separately or with a cyclostationary approach as discussed by Kissner and Guérin [11]. All turbulence components, which are computed by a RANS simulations, are also considered by the 3D-equivalent approach (see section 3.2.1).

3. fRPM-fan method applied to the ACAT1 fan

All fRPM-fan simulations were performed for the ACAT1 fan, which consists of 20 rotor and 44 stator blades. For this fan configuration, a comprehensive measurement campaign was conducted at the Universal Fan Facility for Acoustics (UFFA) test rig at AneCom AeroTest in the framework of the European project TurboNoiseBB. The aim was to record a comprehensive data set for this fan at various operating conditions. In this work, hot-wire data in the fan interstage as well as acoustic measurement data up- and downstream of the fan stage are used. A more comprehensive overview of the measurement campaign was provided by Guérin et al. [34, 35] and Kissner et al. [36]. For more details regarding the hot-wire measurements, refer to Meyer et al. [37]. In-duct acoustic measurements and post-processing methods were presented and described by Tapken et al. [38]. Pereira and Jacob [39] obtained very similar results using their own post-processing treatment.

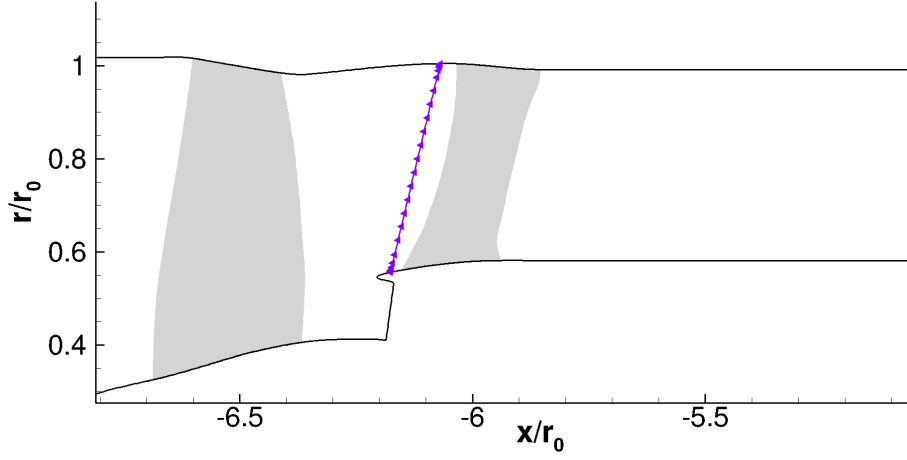
In the following section, the application of the fRPM-fan method to the

ACAT1 fan is described in more detail. In a first step, the RANS simulations, which provide inputs for both 2D and 3D simulation techniques, are presented. In a second step, the setup for the CAA and fRPM methods are discussed. For the 2D simulations, this also includes a brief explanation of the so-called 3D-
255 equivalent approach, which is a technique aimed at setting up 2D simulations that are more representative for the entire fan stage. Lastly, an overview of all fRPM-fan simulations, which are comprised in this paper, is given.

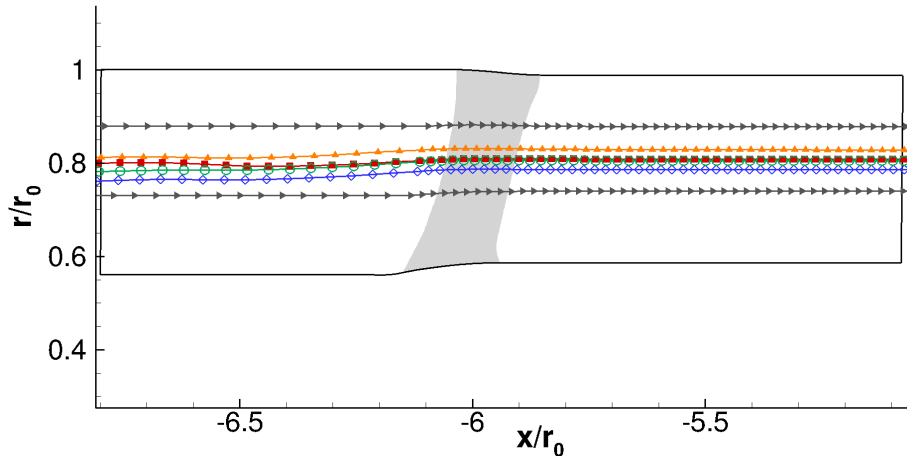
3.1. RANS input calculations

For this paper, all RANS simulations were performed using the DLR in-
260 house CFD solver TRACE [40] and used the Speziale-Sarkar-Gatski/Launder-Reece-Rodi- ω (SSG/LRR- ω) Reynolds stress turbulence model [41]. This turbulence model provides reasonable results for acoustic predictions as discussed by Kissner et al. [36]. An advantage compared to the commonly applied Menter Shear Stress Transport (SST) k - ω turbulence model [42] is that the SSG/LRR- ω
265 Reynolds stress model provides reasonable dissipation rates and therefore reasonable turbulent length scales between the wakes in the fan interstage, even if the ingested inflow turbulence is non-negligible. A mixing plane approach [43] was used. The position of the mixing plane and part of the CFD domain are shown in Fig. 1. The engine support stator vanes in the core duct were
270 neglected.

RANS simulations were performed at three acoustic certification operating points on two different working lines, which correspond to two different rotor loadings: approach (AP) on the Sea Level Static (SLS) and on the Low Noise (LN) working line, cutback (CB) on the SLS working line, and sideline (SL) on
275 the SLS working line. As the atmospheric conditions varied throughout the test campaign, operating points normalized to International Standard Atmospheric (ISA) conditions were prescribed for the RANS simulations (see Table 1). The experimental, normalized mass flows, rotational speeds, and inflow turbulence characteristics were directly applied as boundary conditions. The mesh was
280 adjusted for each operating point to realize measured tip clearances at the rotor



(a)



(b)

Figure 1: (a) RANS domain with mixing plane (purple, left triangle markers). (b) 3D CAA domains shown for full (black) and reduced (grey, right triangle markers) radial domain; streamlines used for 2D simulations at AP SLS (red, square markers), AP LN (blue, diamond markers), CB SLS (green, circle markers), and SL SLS (orange, delta markers).

Table 1: ISA-corrected operating conditions used to initialize and to validate the 3D RANS simulations.

	AP SLS	AP LN	CB SLS	SL SLS
rotor speed (rpm)	3797.6	3797.9	6077.1	6836.7
rotor speed (rpm) [% of speed at design point]	50	50	80	90
bypass mass flow [kg/s]	50.03	53.38	81.50	93.07
core mass flow [kg/s]	6.58	6.56	10.44	11.70
bypass ratio	7.6	8.1	7.8	8.0
rotor tip clearance (LE) [mm]	0.58	0.58	0.44	0.37
rotor tip clearance (TE) [mm]	0.69	0.69	0.46	0.35
inlet turbulence intensity [%]	0.30	0.30	0.20	0.10
inlet integral length scale [m]	0.040	0.040	0.035	0.01
measured bypass FPR	1.108	1.106	1.307	1.410
RANS bypass FPR	1.105	1.104	1.316	1.415
measured core FPR	1.098	1.097	1.266	1.339
RANS core FPR	1.095	1.093	1.257	1.300

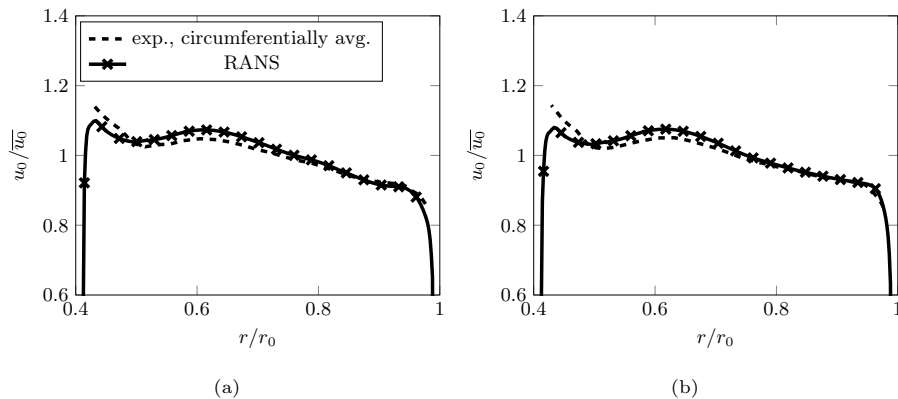


Figure 2: Comparison of the non-dimensional mean flow velocity of the RANS simulation to experimental values in the fan interstage for operating points (a) AP SLS and (b) AP LN.

Leading Edge (LE) and the rotor Trailing Edge (TE). The fan pressure ratio (FPR) of the bypass flow was measured by sensors in the interstage domain of the fan. To ensure comparability, the FPR's were computed analogously for the RANS simulations. Table 1 shows an acceptable agreement between measured and numerically simulated FPR values.

In addition to global performance values, hot-wire data in the interstage domain of the fan stage can also be used to analyze the RANS simulations. Comparison of the circumferentially averaged mean flow velocity u_0 and turbulent kinetic energy k are shown for the approach operating points in Figures 2 and 3. Note that the values are dimensionalized with the respective radially averaged mean flow velocity \bar{u}_0 and the averaged rotor tip radius $r_0 = 0.428$ m. While the mean velocity of the RANS and the hot wire measurements show a reasonable agreement, the discrepancies in terms of the turbulent kinetic energy are more pronounced. Note that the experimental turbulent kinetic energy was multiplied by a factor of 1.5 as suggested by Polacsek et al. [44] to account for the cut-off frequency of the hot wires at about 7 to 8 kHz. For AP SLS, the agreement between hot wire and numerical data is good up to the midspan position. Towards higher radial positions, the circumferentially averaged, experimental values are significantly lower than the numerical values. It can also

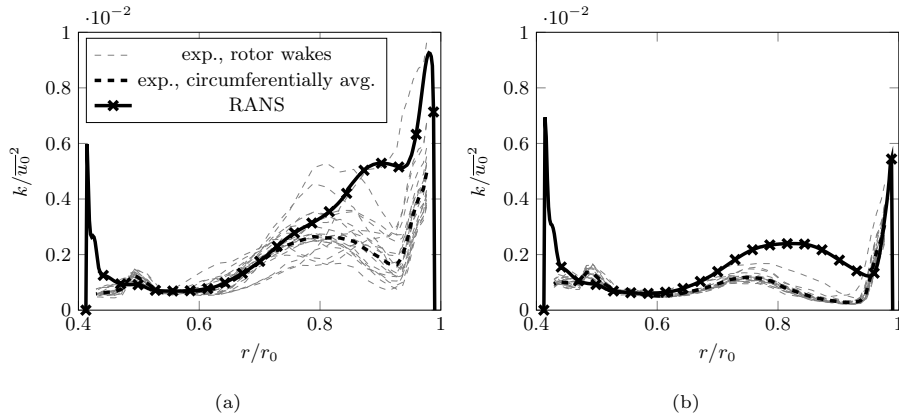


Figure 3: Comparison of the non-dimensional turbulent kinetic energy of the RANS simulation to experimental values in the fan interstage for operating points (a) AP SLS and (b) AP LN.

300 be observed that the wakes of individual rotor wakes vary significantly in the
 experiment. The RANS simulation predicts a severe flow separation at the lead-
 ing edge of the rotor resulting in a thick wake, particularly near the tip wall.
 This leading edge flow separation is visualized in Fig. 4. The streamlines clearly
 indicate a strong vortex structure near the rotor LE at AP SLS resulting in a
 305 thickened boundary layer as indicated by the first axial cut. The pronounced
 wake observed in the interstage of the CFD simulation can therefore be clearly
 attributed to the leading edge flow separation. In the experiment, most rotor
 wakes do not seem to be influenced by such an effect. This discrepancy between
 experiment and simulation was also observed in other studies for this fan at
 310 AP SLS. The RANS benchmark results published by Kissner et al. [36] showed
 that nearly all turbulence models predict a strong leading edge flow separation
 for this operating point. For approach conditions on the LN working line, the
 leading edge flow separation is still present but much less pronounced as can be
 seen by the streamlines and contours in Fig. 4. Thus, the higher bypass flow
 315 stabilizes the off-design operating condition as it enables a reduction in rotor
 loading. As a consequence, the discrepancy between numerical and experimen-
 tal turbulent kinetic energy is smaller at higher radial positions. In addition, the
 individual rotor wakes are more similar for the LN working line (see Fig. 3). Un-

Table 2: Mean flow and turbulence characteristics of the 2D fRPM-fan simulations as determined using the 3D-equivalent approach

	s [%]	$\bar{\rho}_0$ [$\frac{\text{kg}}{\text{m}^3}$]	\bar{u}_0 [$\frac{\text{m}}{\text{s}}$]	\bar{k} [$\frac{\text{m}^2}{\text{s}^2}$]	$\bar{\Lambda}$ [mm]
AP SLS	55.54	1.23	129.06	32.24	5.31
AP LN	50.38	1.22	133.44	20.82	3.83
CB SLS	54.91	1.25	205.89	37.96	3.22
SL SLS	60.75	1.26	231.52	37.71	2.82

fortunately, similar comparisons between hot wire and RANS were not possible
 320 at higher rotational speeds as the hot wire signals were severely contaminated
 by vibrations. However, the RANS simulations do not feature a flow separation
 at the rotor LE as shown in Fig. 4. Based on the observations regarding the
 approach operating points, it is reasonable to think that the discrepancies in
 the interstage turbulence between the experiment and the simulations decrease
 325 as the simulated rotor leading edge flow separation disappears.

3.2. fRPM-fan simulation setups for two- and three-dimensional simulations

This section gives a brief overview of the 3D-equivalent approach. Its aim is
 to enable 2D simulations, which are as representative as possible for the entire
 3D fan stage. In addition, the general setup of 2D and 3D simulations using the
 330 fRPM-fan method is described. Mesh resolution requirements and computation
 costs are also discussed.

3.2.1. 3D-equivalent approach for 2D simulations

The 3D-equivalent approach was recently proposed by Kissner et al. [14]
 in an attempt to make 2D simulations more representative. Instead of av-
 335 eraging results from simulations at multiple radial or streamline positions, the
 3D-equivalent approach determines a streamline whose mean flow characteristics
 correspond to the radially averaged flow characteristics for the 3D duct. The im-
 posed turbulence characteristics are matched to a radially averaged turbulence
 spectrum. In the following section, a brief description is given for completeness

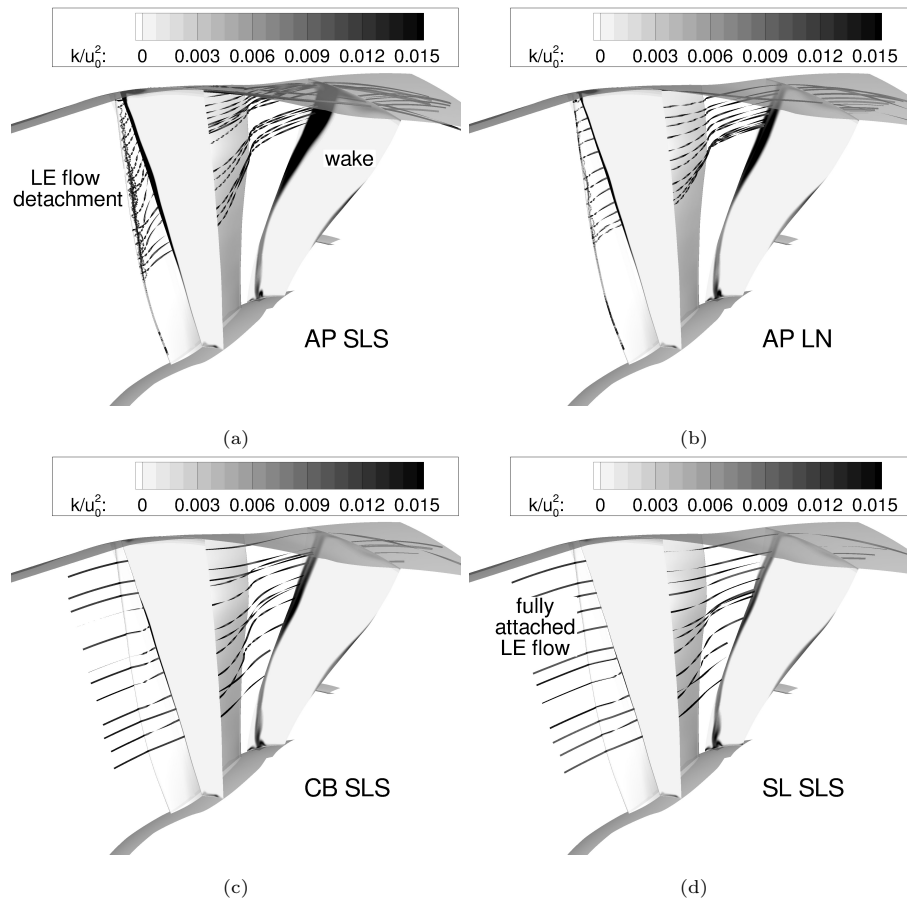


Figure 4: Impact of detached versus fully attached boundary layer flows near the rotor leading edge on the wake structure at an interstage position for operating points (a) AP SLS, (b) AP LN, (c) CB SLS, and (d) SL (bottom right): Streamlines are shown in black and the contour shows non-dimensional turbulent kinetic energies.

340 and to better understand the implication of this approach. The key advantage
of the method is that it should allow for more representative 2D simulations,
which are less dependent on the rotor geometry and on the operating point.
It is a well defined technique and therefore less arbitrary than choosing a ran-
dom streamline position that may have worked in the past for one specific fan
345 and operating point. Applying the technique is also less costly than performing
simulations at multiple streamline positions.

In a first step, flow data are extracted at a cross-section of the duct from
each three-dimensional RANS simulation in the interstage region, preferably
close to the stator leading edge. In this case, the slice is positioned in the
350 bypass duct slightly upstream of the mixing plane, whose position is indicated
in Fig. 1. Since the mixing plane is located close to the stator leading edge and
the turbulence characteristics show an asymptotic behavior with an increasing
distance from the rotor, it can be assumed that the turbulence on that extracted
slice is similar to the turbulence at the stator leading edge, which is relevant for
355 the investigated sound mechanism.

Secondly, mean flow characteristics are circumferentially averaged and cir-
cumferentially averaged turbulence velocity frequency spectra at all radial po-
sitions are computed as follows:

$$S_{22}(f) = \frac{1}{2\pi} \int_0^{2\pi} S_{22}(f, \vartheta) d\vartheta. \quad (1)$$

The turbulent length scale (TLS) and turbulent kinetic energy (TKE) can then
be determined by fitting the circumferentially averaged spectrum to a suitable
target spectrum like a von Kármán spectrum. This spectral averaging tech-
nique [10, 30] has also been applied in past papers to determine turbulence
360 characteristics. Circumferentially averaged mean flow and turbulence charac-
teristics for the different operating points are shown in Fig. 5. The values are
dimensionalized using the respective radially averaged values listed in Table 2.

In the next step, an equivalent flow is determined and matched with the
streamline, which intersects the equivalent radial position at the position of the

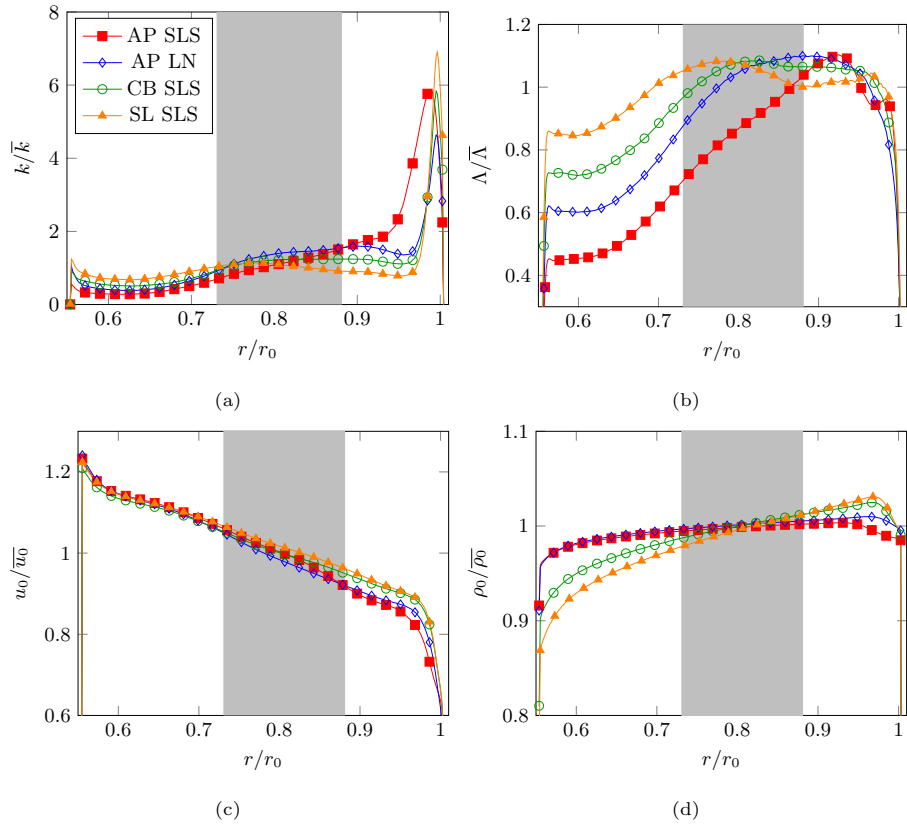


Figure 5: Circumferentially averaged, non-dimensional (a) turbulent kinetic energy, (b) turbulent length scale, (c) mean flow velocity, and (d) mean density on an analysis plane near the stator leading edge. Grey areas indicate the radially reduced domain used for the main 3D simulations.

Table 3: Overall turbulence contributions estimated using the 3D-equivalent approach

	wake turbulence [%]	background turbulence [%]	boundary layer turbulence [%]
AP SLS	73	1	26
AP LN	87	1	12
CB SLS	83	1	16
SL SLS	81	2	17

extraction surface. For analytical formulations of broadband RSI noise, the far field sound can be related to the square of the magnitude of a source term $|\sigma_L|$. If this unsteady loading noise is assumed to be the dominant source, this term can be related to the squares of mean flow velocity and mean density and to the auto-correlation spectrum of the transverse velocity component. The hereafter used proportionality is formulated according to Moreau [45]:

$$S_{pp}(f) \propto |\sigma_L|^2 \propto \rho_0^2 u_0^2 S_{22}(f). \quad (2)$$

For mean flow components involved in this noise source, the following averaging technique was employed:

$$\overline{\rho_0^2 u_0^2} = \frac{1}{n} \sum_{i=1}^n \rho_0(r_i)^2 u_0(r_i)^2, \quad (3)$$

where n is the number of discrete radial positions. For the resulting radially averaged flow $\overline{\rho_0^2 u_0^2}$, the matching streamline position is sought, whereby the matching streamline may not be located within the casing boundary layers. The radially averaged flow characteristics and streamline positions are listed in Table 2. The corresponding streamline positions for the 2D simulations are shown in Fig. 1.

The circumferentially averaged turbulence spectra are radially averaged using Eq. 4, where the weighting is motivated by Eq. 2. Here, it is assumed that the transverse velocity component is the most relevant for noise. This assumption is typically made in analytical models [35] and has also been numerically

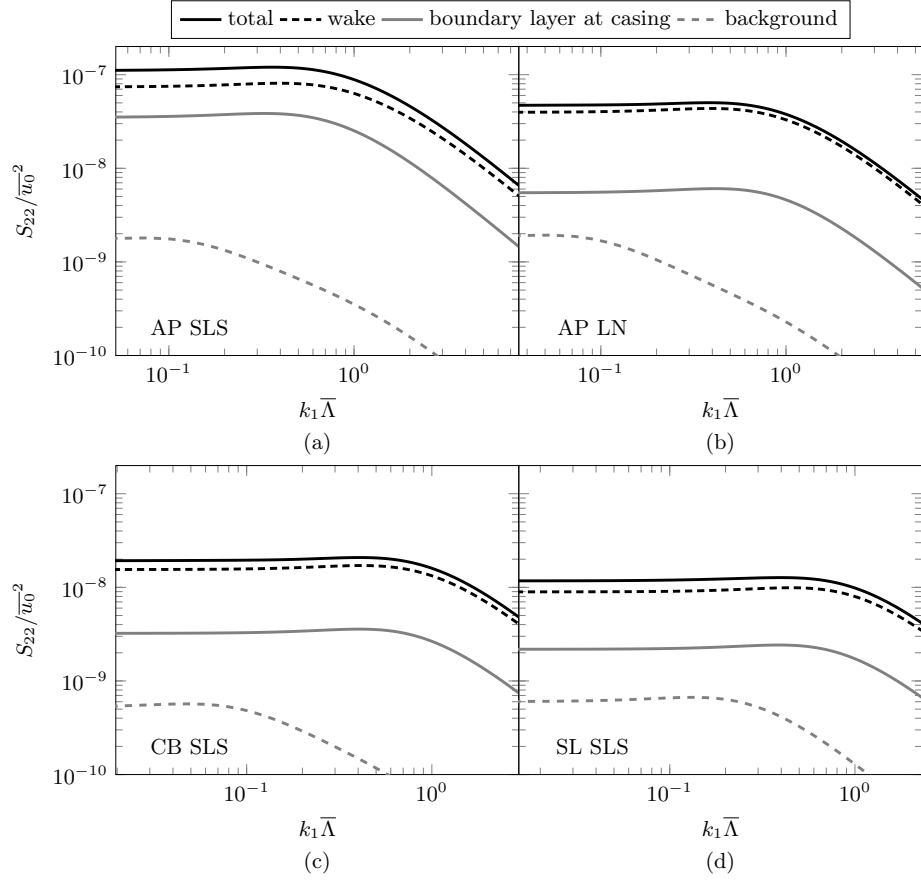


Figure 6: Radially averaged transverse velocity frequency spectra for the total turbulence, the wake turbulence, the boundary layer and boundary layer/tip vortex interaction turbulence, and the background turbulence at the operating points (a) AP SLS, (b) AP LN, (c) CB SLS, and (d) SL SLS.

confirmed for symmetric airfoils [46]. The radially averaged upwash velocity frequency spectrum is determined as follows:

$$\overline{S_{22}(f)} = \frac{\frac{1}{n} \sum_{i=1}^n \rho_0(r_i)^2 u_0(r_i)^2 S_{22}(r_i, f)}{\overline{\rho_0^2 u_0^2}}. \quad (4)$$

Note that the formulation in Eq. 4 is equivalent to performing a mass flow averaging. The total averaged spectra are shown in Fig. 6. For a more in-depth analysis, averaged turbulence spectra can be roughly estimated for each turbulence component - wake, background, or casing boundary layer/tip vortex turbulence - by only considering its respective, relative contribution at each radial position. A threshold TKE, which is related to the prescribed TKE at the inflow of each RANS simulation, is used as the main criterion to distinguish between the different turbulence components. Local turbulence spectra featuring a TKE below the threshold are attributed to the background turbulence component. If the TKE is higher, the turbulence is considered to be wake turbulence, as long as the relative wake width does not span most of the rotor passage. The remaining turbulence spectra are counted as boundary layer turbulence. As a consequence, the boundary layer turbulence component also includes interaction effects between the boundary layer, the tip vortex, and the wake. The spectra for each type of turbulence are shown in Fig. 6 and the relative contributions to the overall turbulence estimated from the respective turbulent kinetic energies related to the radially averaged turbulence spectra of each type of turbulence are listed in Table 3. The spectral shapes and frequency peaks related to the two main turbulence contributors (wake and casing boundary layer) are similar, while the frequency peak of the background turbulence spectrum is shifted to a lower frequency due to the larger TLS of the ingested turbulence. However, since the contribution of the background turbulence is small, the shape of the total spectrum is shaped like a von Kármán spectrum. It is therefore not necessary to consider cyclostationary effects as opposed to the works presented by Kissner et al. [11, 30].

To determine the TKE and TLS of the radially averaged turbulence spectrum $\overline{S_{22}}$, the latter is fitted to a von Kármán spectrum using the previously

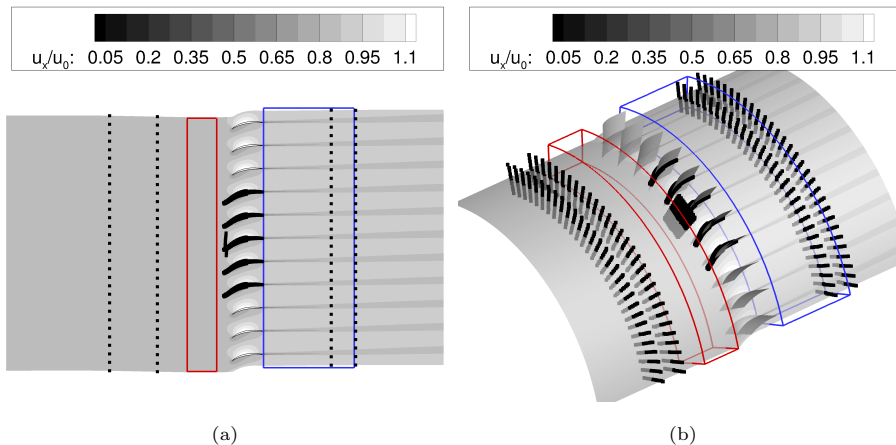


Figure 7: (a) 2D and (b) 3D CAA setups containing 11 stator vanes: Contours show non-dimensional, axial mean flow velocities. Sensor positions are marked in black. The vortex source fRPM patch is shown upstream of the stator row, while the vortex sink fRPM patch is shown downstream of the stator row. In the 3D case, the radial extent of the fRPM patches corresponds to the reduced, radial simulation domain.

determined mean flow velocity u_0 . The resulting values of TKE and TLS are listed in Table 2.

In the last step, the 2D fRPM-fan simulation is set up by using the determined streamline at the position of the radially averaged flow and by prescribing the TKE and TLS values to the turbulence synthesized by the fRPM vortex source. Thus, the simulation is performed using a 3D-equivalent flow and a 3D-equivalent turbulence.

3.2.2. Description of CAA and fRPM simulation setups

This section describes the setup of 2D and 3D simulations for one exemplary operating point and setup design. It includes a general overview of the setup and a discussion of meshing requirements.

General overview. The simulation setups of 2D and 3D simulations are designed as analogously as possible to ensure a fair comparison between the simulations. Nonetheless, 3D simulations require a finer and more high-quality mesh and tend to be more prone to numerical instabilities. They also require a significantly

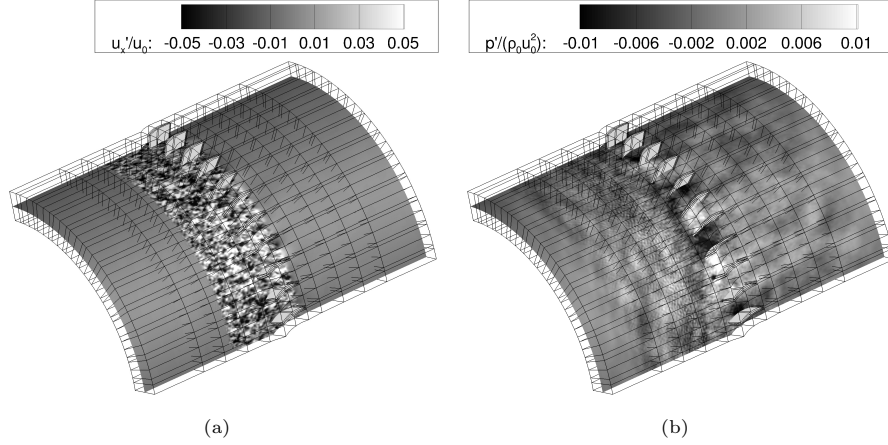


Figure 8: Instantaneous (a) axial velocity fluctuations and (b) pressure fluctuations shown on a radial slice for a 3D simulation with a reduced, radial domain. Contours show non-dimensional, axial fluctuating flow velocities and non-dimensional fluctuating pressures.

higher computational effort. The radial CAA simulation domains are shown in Fig. 1. The setups in Fig. 7 are shown for the AP SLS case. The circumferential domain was reduced from 44 to 11 stator vanes and the radial extent of the 3D domain was reduced to one third of the stator height for 3D most simulations.

415 Note that the 3D setup in Fig. 7 is shown for a simulation featuring a reduced, radial domain. To ensure that the radially reduced domain has representative flow characteristics, the reduced radial domain is centered around the streamline determined with the 3D-equivalent approach for the operating point AP SLS. In addition, the radially averaged transverse frequency spectrum of the radially

420 reduced domain is nearly identical to that of the full domain so that similar results can be expected for both the full and reduced radial domains. Note that all 3D simulations use the same boundary conditions, i. e. the streamlines defining the radial extent of the reduced domain are treated like hub and tip walls. Reducing the domain is an effective way of lowering the computational

425 effort. The implications of these domain reductions are further discussed in the section Appendix C.

In the Fig. 7, the vortex source fRPM patch is outlined in red. The fRPM

patch synthesizes turbulence upstream of the stator leading edges. The turbulence is then injected into the CAA domain through an eddy relaxation term [33] and convected. The turbulence interacts with the blade geometry. Note that the vortex source spans the entire circumference. Therefore, no assumption regarding the acoustic correlation of the blades is necessary as was the case in some previous works [10, 11, 14, 30]. Downstream of the stator vanes, a vortex sink fRPM patch (outlined in blue in Fig. 7) sets the target vorticity to zero, which gradually eliminates the turbulent vortices. As a consequence, the signals at the downstream positioned microphone positions (indicated by the black markers) only contain acoustic velocity perturbations. This is critical for computing the sound power levels using Morfey’s [47] intensity formulation. The evenly spaced sensors up- and downstream of the stator vanes serve to measure emitted in-duct noise in terms of sound pressure and sound power, while the remaining sensors are used to monitor the simulation. Figure 8 shows instantaneous axial velocity fluctuations indicating the synthesized vortices and generated instantaneous pressure fluctuations for the AP SLS case.

As for previous studies [10, 11, 14, 23, 30], precautions were adopted to avoid spurious noise. Viscous wall conditions were used on the blade surfaces to ensure a realistic deformation of the vortices near the blades. This minimizes the direct interaction of the vortices with strong flow gradients at the TE, which can cause artificial noise. Furthermore, sponge zones and an increased cell stretching are employed near the inflow and outflow boundary conditions to avoid reflections.

As the 3D simulations tend to be more prone to numerical instability, further measures were introduced. Instabilities can arise at the hub and tip walls, particularly in areas featuring high velocity gradients or in proximity of the vortex source fRPM patch. To suppress these issues, inviscid wall conditions were applied at the hub and tip walls and the mean velocities at the wall nodes were set equal to their radially adjacent nodes. This was the only necessary modification applied to the mean flow. Note that the boundary layer is still present as only the cells directly at the wall were modified and flow gradients related to the boundary layer are still present in the nodes close to the hub and tip walls.

In especially critical areas, damping spots featuring a Gaussian shape defined
460 by a half-value radius and a relative damping magnitude were also introduced
at specified positions. By using damping spots rather than introducing a global
damping, the simulated solution is only modified very locally and the impact on
the overall solution is smaller. The implication of using these damping points
will be discussed during the course of this paper. A further challenge is that the
465 fRPM patch does not "know" the boundary conditions of the CAA domain. A
direct intersection of the vortex source with the wall and periodic boundary con-
ditions therefore causes spurious noise. As a consequence, the outermost cells
in circumferential and radial directions were removed. In addition, the forcing
factor was set to zero in the three radial fRPM nodes closest to the upper and
470 lower boundary surfaces of the radially truncated domain. For the vortex sink
patch, the outermost cells in the direction were also removed as the interaction
of the wall conditions with the vortex sink partly blocked the emitted sound
downstream of the stator vanes. These precautions enabled stable 3D simula-
tions without falsifying or simplifying the physical problem. It should be noted
475 that many of these problems are not unique to the fRPM-fan method. In fact,
Polacsek et al. [44] also reported difficulties with flow gradients and spurious
noise for their 3D simulations and introduced appropriate measures to achieve
a numerically stable computation.

Mesh resolution. The chosen mesh resolution is an important driver for the
480 computational cost of a simulation. The goal of the mesh design is therefore
to create a mesh, which meets accuracy targets with the least amount of com-
putational effort. Two key ingredients need to be considered for dimensioning
the mesh: turbulence and acoustics. The turbulent vortices need to be well re-
solved upstream and in the proximity of the stator vanes. Acoustic criteria are
485 crucial in the entire domain, except near the in- and outlet boundaries, where
cell stretching and damping are applied to eliminate reflections at these bound-
ary conditions. The chosen target frequency of the 3D simulations was 10 kHz,
while 20 kHz were chosen for the 2D simulation setups. 3D simulations were

Table 4: Comparison of mesh resolutions in all spatial directions with respect to the target frequency of each simulation and total mesh sizes per stator passage

	$\widetilde{\frac{\lambda_{-x}}{\Delta x_-}}$	$\widetilde{\frac{\lambda_{+x}}{\Delta x_+}}$	$\widetilde{\frac{\lambda_{r\theta}}{\Delta r}}$	$\widetilde{\frac{\lambda_r}{\Delta r\theta}}$	n_{passage}
3D, AP SLS, red. domain	14.6	29.6	32.5	54.1	665,712
3D, AP SLS, full domain	14.6	29.6	32.5	54.1	2,544,128
2D, AP SLS	9.2	8.8	-	22.8	51,400
2D, CB SLS	8.6	10.3	-	23.8	63,744
2D, SL SLS	7.9	10.8	-	26.2	86,320

only performed at approach operating points, whereas 2D simulations were also
490 performed for the sideline and cutback operating points, whose frequency peaks
are expected to be shifted towards higher frequencies as can be inferred from
the transverse velocity frequency spectra shown in Fig. 6.

To determine the maximum permissible cell size with respect to all spatial
directions (Δx_+ , Δx_+ , Δr , and $\Delta r\theta$) for a specific target frequency, the prop-
495 erties of all sonic eigenmodes capable of propagating within the computational
domain were computed up- and downstream of the stator vanes. For the 3D
simulations, a plug flow assumption was used. While this is a valid assumption
for the flow downstream of the stator vanes, it is a bit questionable for the up-
stream direction. However, turbulent resolution requirements are more stringent
500 for a low-speed operating point like approach, which determine the mesh reso-
lution upstream of the stator vanes. For the 2D simulations, a relatively simple
rigid body swirl formulation was used, where the azimuthal modes are the only
relevant eigenfunctions. This approach for designing 2D meshes was discussed
in more detail by Kissner et al. [14]. For the high-speed operating points of
505 CB and SL, the acoustic mesh resolution requirements are more restrictive than
turbulent mesh resolution requirements. The wavelengths of all cut-on acoustic
modes in the target frequency range were resolved with at least 7 points per
wavelength (PPW) in all spatial directions. This complies with the theoretical
resolution limit of 5.4 PPW for a Dispersion-Relation-Preserving scheme [48].

510 To synthesize a realistic turbulence spectrum like a von Kármán spectrum,
Gaussian filters are superposed to approximate a target spectrum. In order
to determine the computationally most efficient settings in terms of number of
filters, cell sizes, and Gaussian length scales, an optimization routine was in-
troduced by Kissner and Guérin [23]. The routine uses inputs like turbulence
515 and flow characteristics, the maximum permissible cell size for acoustic reso-
lution, the maximum target frequency, and a maximum deviation between the
target and synthesized spectra to compute efficient settings. The routine relies
on findings from parameter studies regarding the computational effort and pa-
rameter constraints to ensure meaningful outcomes of the routine. The method
520 was applied for 2D and 3D simulations. For 3D simulations, multiple radial
positions were considered. Mesh resolutions and mesh sizes are listed in Ta-
ble 4. The mesh resolutions are given as median points per wavelengths in all
spatial directions. The median value was computed with respect to all cut-on
eigenmodes at the target frequency (10 kHz for 3D simulations, 20 kHz for 2D
525 simulations). These values are conservative estimates as the resolution is com-
puted in terms of the critical cell sizes, whereas the actual cell sizes are smaller.
Furthermore, a median instead of a mean value was chosen as it minimizes the
contribution of high wavelengths near the cut-on criteria. It can be seen that
the mesh resolution requirements are more stringent for 3D simulations as all
530 cut-on modes have to be fully resolved in all spatial directions at each radial
position. Note that the same meshes were used for both AP operating points
as the mesh resolution requirements are similar and only the values for AP SLS
are included in Table 4. The approach simulation settings and meshes of the 3D
simulations in this work are similar to those discussed by Kissner and Guérin
535 [23]. In that paper, the authors also presented a mesh study, which indicated
that the chosen mesh resolution was suitable.

3.3. Test matrix of fRPM-fan simulations

Fourteen different simulations including eight 3D and six 2D simulations are
discussed in this paper. Details regarding the simulations are listed in Table 5.

⁵⁴⁰ The simulation numbers are used in the following figures and in the subsequent text as an addition to more intuitive descriptors in order to unambiguously identify referenced simulations.

Table 5: Test matrix of performed simulations

	dimension	operating point	radial turbulence profile	number of stator vanes	radial extent	damping magnitude at casing
1	3D	AP SLS	constant	11	reduced	0.2
2	3D	AP LN	constant	11	reduced	0.2
3	3D	AP SLS	varying	11	reduced	0.2
4	3D	AP SLS	constant	11	reduced	0.3
5	3D	AP SLS	constant	11	reduced	0.5
6	3D	AP SLS	constant	11	reduced	0.7
7	3D	AP SLS	constant	11	full	0.5
8	3D	AP SLS	varying	5	full	0.5
9	2D	AP SLS	-	11	-	-
10	2D	AP LN	-	11	-	-
11	2D	CB SLS	-	11	-	-
12	2D	SL SLS	-	11	-	-
13	2D	AP SLS	-	5	-	-
14	2D	AP SLS	-	44	-	-

The main focus of this paper is to directly compare 2D and 3D simulations at the two approach operating points. The main simulations are therefore simulations 1, 2, 9 and 10, which all contain 11 stator vanes. Notice that the most relevant 3D simulations were performed with constant turbulence characteristics, which are identical to those determined by the 3D-equivalent approach for the 2D simulations. This simplifies the comparison between 2D and 3D simulations but also inherently contains the assumption that the 3D-equivalent approach is reasonable. To check this assumption, simulation 3 was performed. It features radially varying turbulence characteristics, which were directly extracted from the RANS simulation and circumferentially averaged. It is expected that this simulation produces similar results to simulation 1. The reduced radial domain was also extracted with the 3D-equivalent approach in mind: To ensure representative flow characteristics, the reduced radial domain is centered around the streamline used for simulation 9. To ensure representative turbulence characteristics, it was verified that the radially averaged transverse velocity spectra of the reduced and full radial domains are nearly identical. The radially reduced domain is convenient for parameter studies since the computational effort is significantly reduced. Simulations 7 and 8 were performed to verify that the setup spanning the entire stator domain produces similar results as the radially reduced domain. Simulation 8 is also useful in assessing the consequences of reducing the computational domain in circumferential direction as it contains fewer vanes. To check whether the findings also hold true for 2D simulations, two additional simulations featuring 5 (simulation 13) and 44 stator vanes (simulation 14) were performed at operating point AP SLS. As discussed in the above section 3.2.2, damping spots were introduced at the hub and tip walls. Their impact was analyzed by performing different simulations (4-6) with varying relative damping magnitudes. Finally, to demonstrate that the simulation approach is in principal also applicable for high-speed operating points, 2D simulations were performed at cutback (simulation 11) and sideline (simulation 12) conditions.

All 2D simulations were resolved up to a target frequency of 20 kHz. They

were performed on a small cluster computer featuring Intel(R) Xeon(R) CPU
575 E7-4830 v3 @ 2.10GHz CPU's but can technically also be performed within a few
hours on a regular computer. The simulation time scaled linearly as the number
of grid points per processor was similar. It ranged from 6.9 to 10.1 CPU hours
per 100,000 grid points per 100,000 time steps. Since 2D simulations are cheap,
longer sampling times resulting in smoother spectra were used, yet 100,000 time
580 steps are enough to achieve convergence in terms of spectral shapes and levels.
The 3D simulations have a mesh resolution limit of 10 kHz and were computed
within a few days on the modern HPC (High Performance Computing) DLR
cluster CARA (Cluster for Advanced Research in Aerospace), which features
AMD EPYC 7601 32-Core processors. The computing time ranged between
585 94.9 and 99.7 CPU hours per 100,000 grid points per 100,000 time steps. Since
the 3D simulations are more expensive, shorter sampling times were used.

4. Comparison of two- and three-dimensional simulation results

The following section focuses on the comparison of 2D and 3D simulation
results at two approach operating conditions on two different working lines. The
590 simulations were set up as analogously as possible. The following observation –
see justifications in the appendix – were made:

- In accordance with the proposed 3D-equivalent approach, both constant
(determined with the 3D-equivalent approach) and radially varying tur-
bulence characteristics (directly extracted from RANS) produce the same
595 results for 3D simulations.
- The use of local damping spots at hub and tip walls of 3D simulation
domains has a limited influence on predicted fan broadband noise levels.
- The reduction of the radial domain to about one-third of the stator domain
has a limited impact on the results of the 3D simulations.
- 600 • Simulations containing only 11 stator vanes instead of the full 44 stator
vanes are capable of producing reliable results.

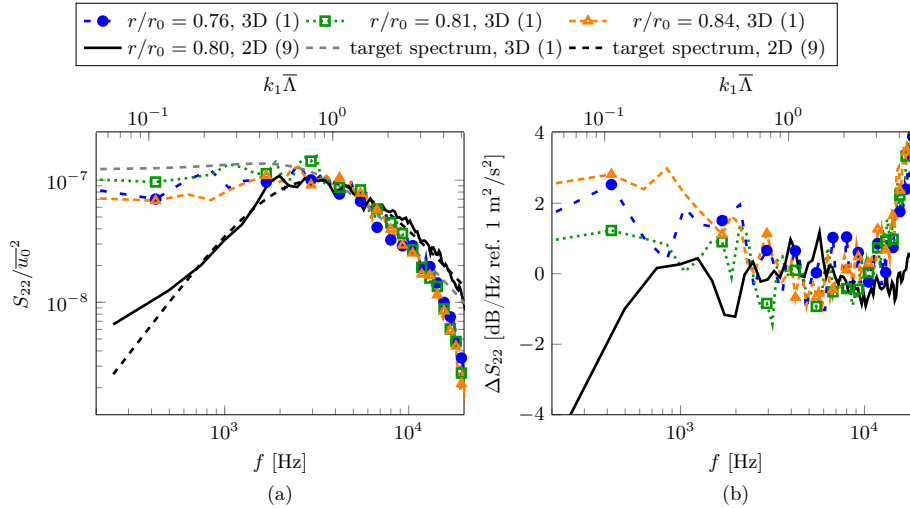


Figure 9: Comparison of (a) transverse velocity frequency spectra and (b) offsets at selected radial positions.

The section is structured as follows: In a first step, the turbulence realization is briefly discussed. In a second step, the numerical data are compared to experimental data in terms of in-duct sound power and sound pressure. Lastly, corrections for 2D simulations are formulated to address observed discrepancies between 2D and 3D simulation results.

4.1. Turbulence realization

The turbulence realization of the simulations is verified at a position near the stator leading edge. For the AP SLS operating point, the numerically realized transverse velocity frequency spectra of the 2D and 3D simulations are compared to the target spectra on the left hand side of Fig. 9. For the 3D simulations, only a few radial positions are shown and the target spectra at all positions are nearly identical due to the use of constant turbulence characteristics. The 3D simulation tends to underestimate the target turbulence at low frequencies, while the agreement is quite satisfactory at higher frequencies up to the target frequency of 10 kHz. The 2D spectrum differs in shape, which is in agreement with the theory as formulated by Pope [57]. Related formulas for the von

Kármán spectrum are listed in the appendix (compare Eq. D.4 and Eq. D.7). The agreement between target and realized spectra is good over a majority of the frequency range up to the target frequency of 20 kHz. However, the realized turbulence levels at very low frequencies are higher than the targeted levels. This seems to be a convection effect as this feature develops with an increasing distance from the vortex source fRPM patch. It should also be noted that very low levels and steep gradients as for the 2D spectra at low frequencies are generally more challenging to realize. The observed trends are similar for the other 2D and 3D simulations, which were performed for this paper. Since the main goal of this paper is to compare 2D and 3D simulation results, the discrepancies in the turbulence realization, particularly at low frequencies, have to be considered. To compensate for these differences, the spectral offsets (see right hand side of Fig. 9) between target and realized spectra are added to the sound pressure and sound power level spectra. This correction technique assumes that the transverse velocity frequency spectrum is the most relevant fluctuating velocity component for this sound source. This method was also applied in a previous paper [14].

4.2. Comparison to experimental results

Numerical sound pressure and sound power levels were computed at sensor positions up- and downstream of the stator row and corrected in terms of their respective turbulence realizations as discussed in the preceding section. While a simple averaging is applied to compute the sound pressure levels, the numerical sound power levels were computed by weighting the intensity spectra at each sensor position by an appropriate elemental area.

Comparisons of numerical and experimental sound pressure and sound power levels up- and downstream of the stator vanes are shown in Figures 10 and 11. The spectra are shown relative to the frequency f and the Helmholtz number $\kappa_0 r_0$, which is defined in terms of the free-field acoustic wavenumber and the rotor tip radius. The speed of sound was assumed to be similar for all operating points and was set to ISA conditions: $c_0 = 340.3$ m/s.

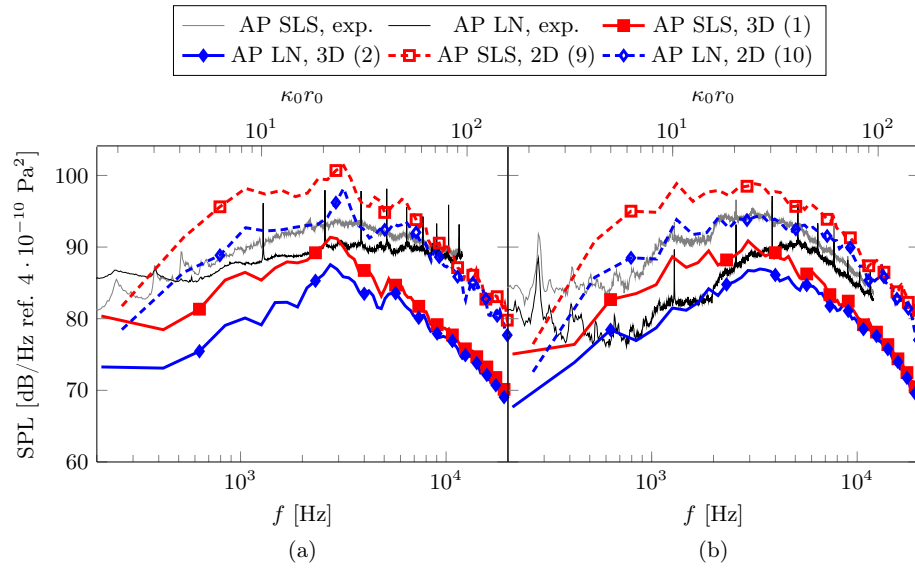


Figure 10: Comparison of experimental and numerical sound pressure levels (a) up- and (b) downstream of the stator vanes.

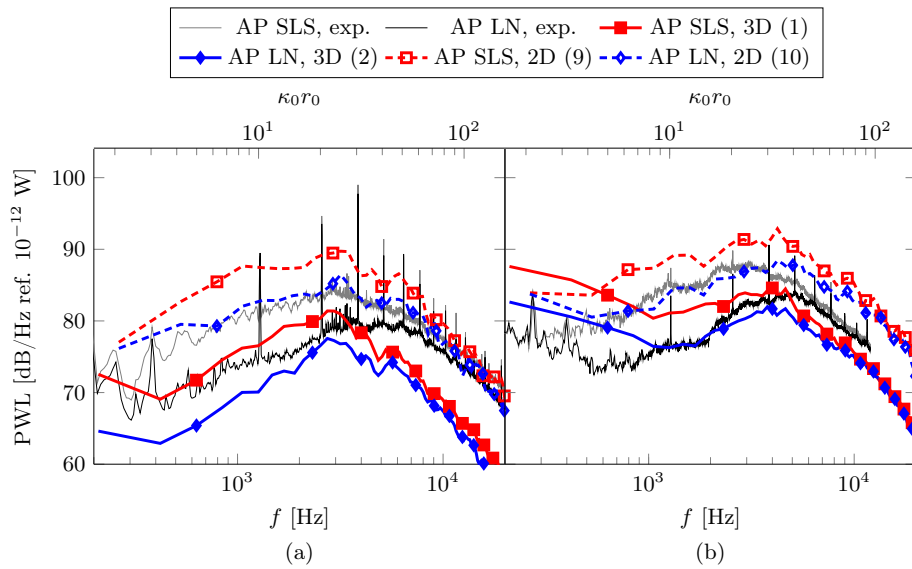


Figure 11: Comparison of experimental and numerical sound power levels (a) up- and (b) downstream of the stator vanes.

The downstream, experimental values were determined with the so-called WaveNumber Decomposition (WND) method using signals from a linear sensor array of microphones flush-mounted on the outer casing wall of the bypass duct. This method allows for the separation of acoustic and hydrodynamic pressure fluctuations [49], tones were removed [50], and an equal energy density distribution between propagating modes of the same frequency band was assumed [51]. The upstream sound power levels were directly determined by integrating over a far-field array composed of 25 microphones, which were positioned at equidistant polar angles. No assumption regarding the modal energy distribution is necessary but tones are still present. In-duct upstream sound pressure levels were determined by applying the Azimuthal Mode Analysis (AMA) method at a ring sensor array positioned in the inlet duct. Further details regarding the AMA measurements can be found in a study by Behn et al. [52]. Note that the AMA measurements are prone to uncertainty as the method cannot separate hydrodynamic from acoustic pressure fluctuations and no distinction between up- and downstream propagating modes can be made. Some signal contamination, particularly at low frequencies, is therefore expected. It should also be noted that the measurements inherently contain rotor blockage effects, while the numerical data does not consider these. Guérin et al. [35] postulated that the measurements contain at least two major broadband noise sources: one at lower frequencies and one at higher frequencies, which is mostly due to broadband rotor-stator-interaction noise. It is thought that the self-noise of the test rig may play a role, especially at lower frequencies, and it could also be that there are additional, less prominent broadband noise sources contained in the spectrum, which cause increased levels.

The Figures 10 and 11 show that the 2D and 3D numerical results have a similar shape but the absolute levels do not match. It should be recognized that the increase in 3D sound power levels at low frequencies is probably related to some remaining vortices in the simulation domain, as it can be challenging to completely eliminate large-scale turbulent structures within a limited axial space using the eddy relaxation technique. While the 2D results overpredict

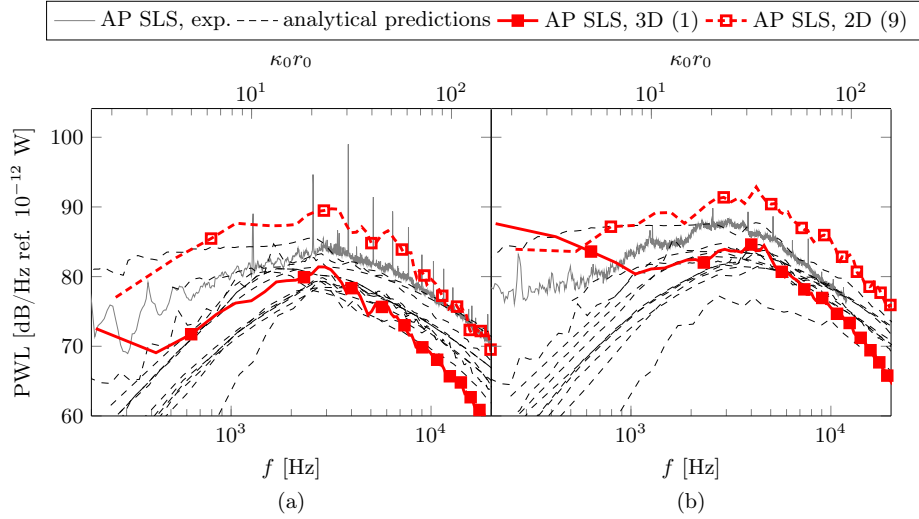


Figure 12: Comparison of experimental, analytical [35] and numerical sound power levels (a) up- and (b) downstream of the stator vanes.

the experimental levels, the 3D results tend to underestimate the experimental
680 levels. In Fig. 12, the numerical results are compared to predictions issued
from a benchmark of analytical methods shown and discussed by Guérin et al.
[35]. While the RANS inputs were different, this aspect is likely negligible [36].
Like the 3D results, the analytically predicted sound power levels tend to be
lower than the experimental values. In fact, an underestimation of sound power
685 and sound pressure levels was consistently reported for analytical methods [34–
36, 53], synthetic turbulence methods [23, 44, 54], and scale-resolving methods
[55] for this fan operating the approach point on the SLS working line. In
conclusion, the 3D results are likely more realistic than the 2D results.

To further compare the numerical and experimental results, the trends of the
690 operating point AP LN with respect to the operating point AP SLS are shown in
Fig. 13. While the absolute levels of the sound power and sound pressure of the
2D and 3D simulations deviate significantly, the 2D and 3D trends are nearly
identical. In addition, the numerical and experimental trends are quite similar.
The larger discrepancies between the experimental sound pressure levels may

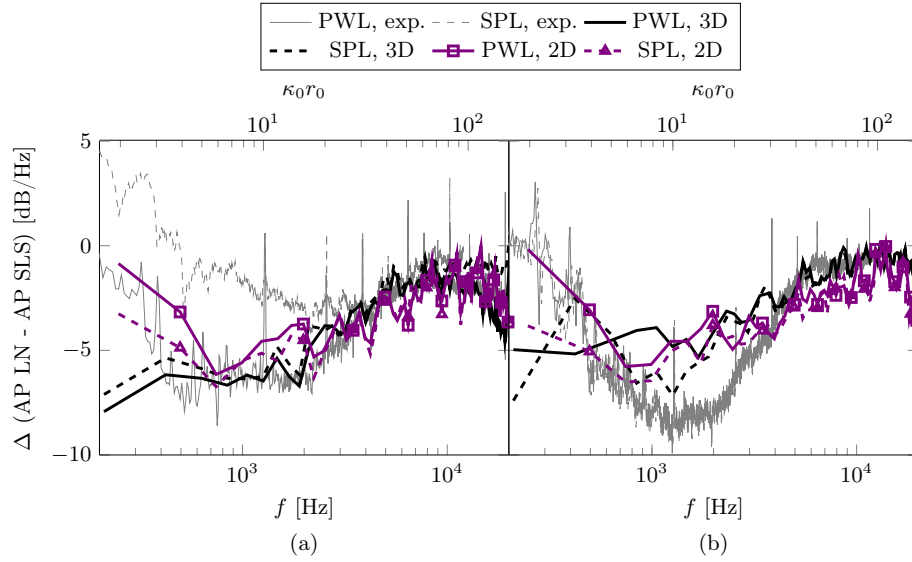


Figure 13: Comparison of numerical and experimental trends (a) up- and (b) downstream of the stator vanes for the operating point AP LN.

695 be an artifact of the AMA method as discussed in the preceding paragraphs. At higher operating speeds, the overall trends between 2D numerical results and experimental values are also quite satisfactory as can be seen in Figures E.22 and E.23. While the absolute levels do not agree perfectly, the differences are well reproduced by the simulations.

700 4.3. Correction of two-dimensional results

In this section, the 2D and 3D results are discussed in terms of the sound pressure level spectra and a suitable correction technique is proposed.

As observed in the previous section, the spectral shapes are similar but there seems to be an offset in the absolute levels. For clarity, the numerical sound pressure levels are shown without any experimental values in Fig. 14. To explain these discrepancies, a correction addressing two different aspects regarding the differences in 2D and 3D simulations is applied.

The first relevant factor is that the 2D and 3D turbulence realization differs in terms of the transverse velocity component as can be seen in Fig. 9. As the

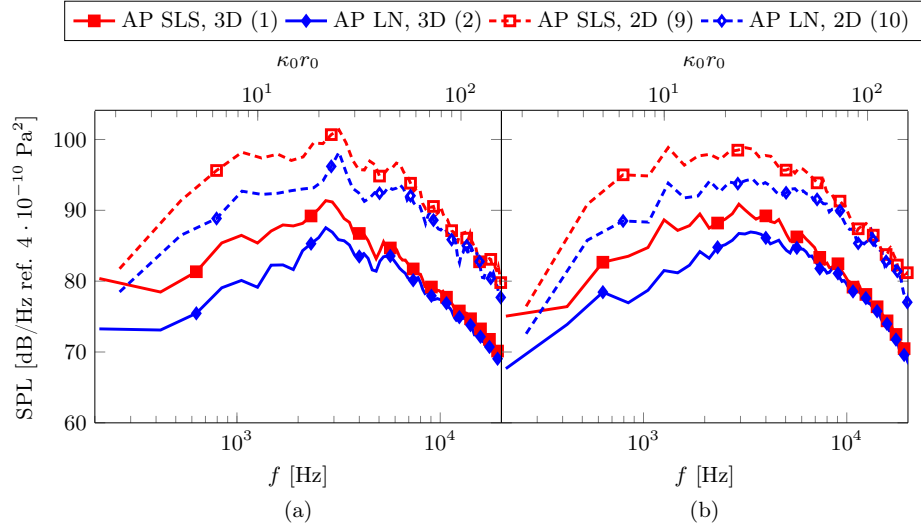


Figure 14: Comparison of 3D and 2D sound pressure levels (a) up- and (b) downstream of the stator vanes.

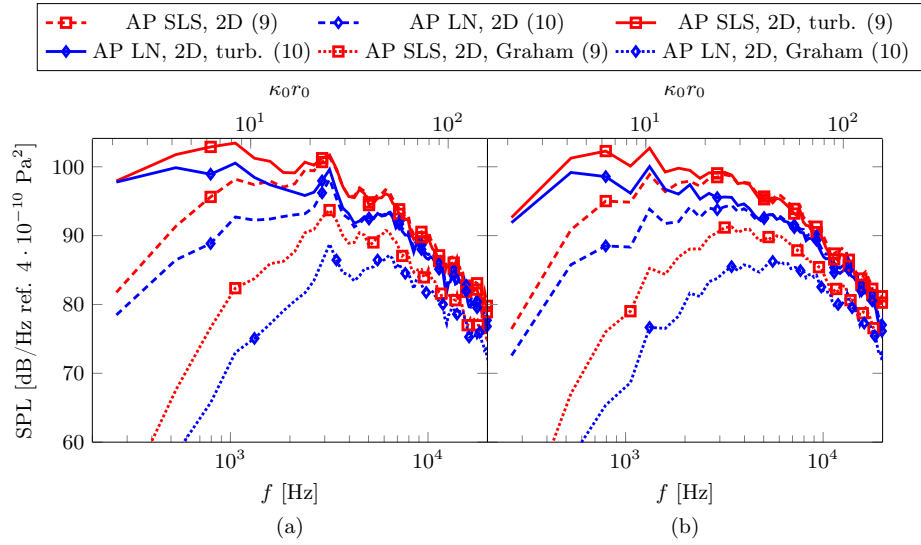


Figure 15: Impact of the correction for the difference in spectral shape of the transverse velocity spectra (Eq. 5, solid lines) and the correction based on Graham's similarity rules (Eq. 9, dotted lines) on 2D sound pressure levels (a) up- and (b) downstream of the stator vanes.

transverse velocity component is the most relevant for fan broadband noise, the correction needs to consider this difference in spectral shape:

$$\frac{S_{pp}^{3D}}{S_{pp}^{2D}} \sim \frac{\Phi_{22}^{3D}(k_1)}{\Phi_{22}^{2D}(k_1)}, \quad (5)$$

where the definitions of the transverse wavenumber spectra for the von Kármán spectrum can be found in the appendix (see Eq. D.4 and Eq. D.7). This type of correction was first proposed by Wohlbrandt et al. [10] and causes an increase of the 2D levels at low frequencies, while the levels at mid and high frequencies are only slightly decreased as can be seen in Fig. 15. Note that all one-dimensional, two-sided velocity wavenumber spectra can be easily converted into one-sided velocity frequency spectra, which have been previously used in this paper: $S_{ii}(f) = 2\Phi_{ii}(k_1) \frac{2\pi}{u_0}$, where u_0 is the mean total velocity.

The second relevant aspect is related to Graham's similarity rules [21]. Only turbulent waves, whose wave fronts have a supersonic trace velocity, are able to generate sound capable of propagating within the duct. Supercritical waves fulfill the criterion:

$$k_3 < \frac{\kappa_0}{\beta}, \quad (6)$$

where the acoustic wavenumber κ_0 can be expressed in terms of the Mach number and the turbulent streamwise wavenumber component ($\kappa_0 = |k_1|M$) and the compressibility factor β is given as $\beta = \sqrt{1 - M^2}$. Since the stator blade features a sweep of about $\gamma \approx 15^\circ$, the radial wavenumber can be defined as suggested by Glegg [22] and successfully applied e. g. by Clair et al. [56]:

$$k_{3,\gamma} = \frac{k_1 M^2}{1 - M^2} \tan(\gamma) + k_3. \quad (7)$$

The cut-on criterion can therefore be reformulated as follows:

$$k_3 < \frac{\kappa_0}{\beta} \left(1 - \frac{M \tan(\gamma)}{\beta} \right). \quad (8)$$

While the 3D simulations inherently contain this physical mechanism and any sound emission due to subcritical gusts dissipates quickly, this is not the case for 2D simulations. For 2D simulations, all incoming turbulent waves create

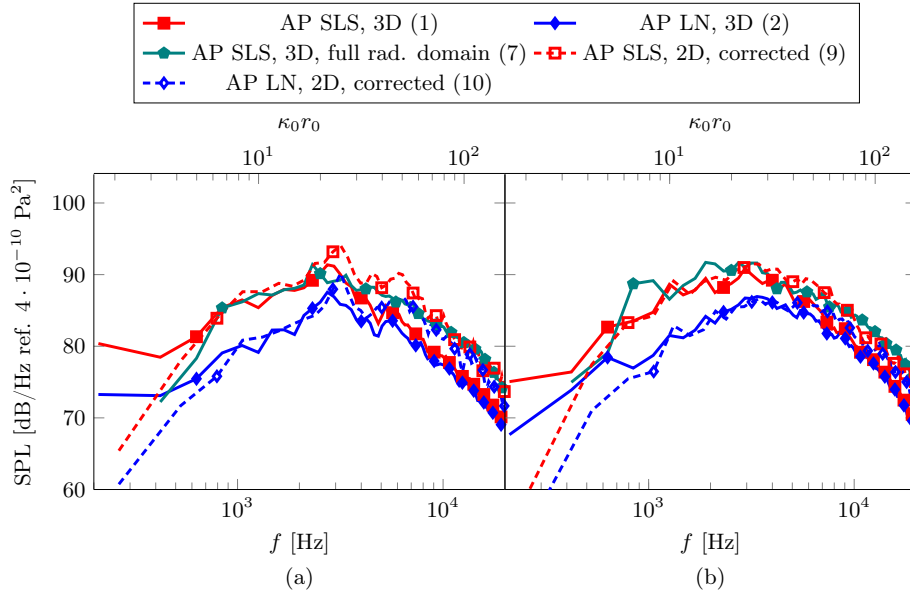


Figure 16: Comparison of 3D and corrected, 2D (Eq. 10) sound pressure levels (a) up- and (b) downstream of the stator vanes.

sound, which causes the emitted sound pressure in the duct to be higher than can be expected in reality. In addition, no sweep can be considered. Another correction can therefore be introduced:

$$\frac{S_{pp}^{3D}}{S_{pp}^{2D}} \sim \frac{2 \int_0^{\frac{\kappa_0}{\beta} \left(1 - \frac{M \tan(\gamma)}{\beta}\right)} \Phi_{22}^{3D}(k_1, k_3) dk_3}{\Phi_{22}^{3D}(k_1)}. \quad (9)$$

The exact derivation of the integration for the von Kármán spectrum can be found in the appendix (see Eq. D.8). A similar correction was also applied by e. g. Blázquez and Corral [12] to discard the contribution of subcritical, turbulent waves, although they did not consider blade sweep. However, the impact of considering blade sweep at low Mach numbers is small for the moderate sweep angle of this fan configuration. The correction (Eq. 9) causes a decrease in the overall sound pressure levels as can be seen in Fig. 15. The correction has a stronger influence at lower than at higher frequencies. It reduces the number of total cut-on modes, therefore causing a reduction in emitted noise levels.

When the two aspects are combined, the following correction factor can be

defined:

$$\frac{S_{pp}^{3D}}{S_{pp}^{2D}} \sim \frac{2 \int_0^{\frac{\kappa_0}{\beta} (1 - \frac{M \tan(\gamma)}{\beta})} \Phi_{22}^{3D}(k_1, k_3) dk_3}{\Phi_{22}^{2D}(k_1)}. \quad (10)$$

725 This correction factor considers the difference in spectral shape of the 2D and 3D transverse velocity spectra and discards subcritical turbulent waves, which are not capable of propagating efficiently within a 3D duct. Using the correction in Eq. 10, Fig. 16 now shows a reasonable agreement between the corrected, 2D and the 3D results for most of the frequency range and a significant improve-
 730 ment can be achieved compared to the initial results shown in Fig. 14. At the lowest frequencies, the corrected, 2D results underestimate the 3D results. At the highest frequencies, the 2D results slightly overpredict the 3D results. However, this can largely be attributed to the reduction of the radial domain and the increased attenuation due to the local damping spots as the comparison to
 735 3D results over the full radial domain are in even better agreement with the corrected, 2D results. The impact of the reduction of the radial domain and of damping spots are further discussed in sections Appendix B and Appendix C. The corrected, 2D results are also compared to experimental and analytically predicted sound power levels in the appendix (see Figures F.24, F.25, and F.26).
 740 All spectra are within an expected range and it can be shown that blade sweep becomes increasingly important for increasing rotational speeds. It should be noted that this proposed correction assumes that the sound propagation produces similar pressure levels for a 2D and a 3D duct. In reality, this is not true at low frequencies due to the reduced number of acoustic propagating modes.
 745 However, the hypothesis becomes valid as the number of acoustic cut-on modes is statistically large. It also assumes the 2D and 3D blade response are – on average – comparable.

The correction factor in Eq. 10 can be related to existing correction techniques, when blade sweep is neglected. For low Mach numbers, it can be shown that the following relationship holds true:

$$\int_0^{\kappa_0/\beta} \Phi_{22}(k_1, k_3) dk_3 \sim \kappa_0 \Phi_{22}(k_1, k_3 = 0). \quad (11)$$

Thus, the correction factor in Eq. 10 can be related to Dieste’s [16] and Hainaut’s [17] corrections, if the terms related to the distance of sound propagation are neglected. Both corrections are Amiet-based [15] formulations. For low Mach numbers, the following relationship exists:

$$\frac{S_{pp}^{3D}}{S_{pp}^{2D}} \sim \frac{2 \int_0^{\kappa_0/\beta} \Phi_{22}^{3D}(k_1, k_3) dk_3}{\Phi_{22}^{2D}(k_1)} \sim \frac{2\kappa_0 \Phi_{22}^{3D}(k_1, k_3 = 0)}{\Phi_{22}^{2D}(k_1)} = \frac{\Phi_{22}^{3D}(k_1) 2\kappa_0 l_3}{\Phi_{22}^{2D}(k_1) \pi}, \quad (12)$$

where l_3 is the acoustic correlation length in the radial direction. The definition of l_3 for von Kármán turbulence was e. g. given by Amiet [15]. Dieste’s formulation inherently contains both a correction of 2D versus 3D spectral shapes of the transverse velocity component and considers only supercritical turbulent waves. Hainaut’s formulation $\frac{2\kappa_0 l_3}{\pi}$ is essentially a simplified version of Dieste’s correction, which assumes that 2D and 3D turbulence realizations are identical. Both corrections can be seen as low-speed approximations for the proposed correction in Eq. 10, which both considers differences in 2D versus 3D turbulence realization and discards subcritical turbulent waves. This relation to previously applied, Amiet-based correction techniques further confirms that the proposed correction approach is reasonable.

5. Conclusion

This paper presented a study based on 2D and 3D fRPM-fan simulations at different operating points of the ACAT1 fan. The focus of this paper was to compare the 2D and 3D approaches and to formulate a suitable correction technique for 2D results.

Both 2D and 3D approaches are capable of reproducing experimental trends. The sound power level spectra obtained with the 3D simulation approach were found to be consistent with previous findings reported in numerous works, which showed that the predicted levels are typically lower than the measured levels for this fan. To perform 2D fRPM-fan simulations, which are as representative as possible for the entire fan geometry, the so-called 3D-equivalent approach was applied. This approach selects a streamline featuring representative mean flow

characteristics and prescribes turbulence characteristics determined by fitting a radially averaged upwash velocity frequency spectrum to a reasonable target spectrum like a von Kármán spectrum. While the raw 2D sound power and sound pressure level spectra were similar in shape as the 3D spectra, the absolute levels were significantly overestimated. To rectify this issue, a correction technique was proposed, which addresses two separate physical aspects:

1. The critical transverse velocity spectrum differs for 2D and 3D turbulence in terms of its spectral shape.
2. Only turbulent gusts featuring a supersonic trace velocity generate sound, which can propagate in a duct. Due to the absence of the third dimension, this physical mechanism cannot not be captured by 2D simulations.

This correction technique lowered the absolute spectral levels and a good agreement between 2D and 3D results was achieved. The similarities to other commonly used correction techniques reiterate its suitability.

For this fan configuration, the 2D fRPM-fan method in combination with the 3D-equivalent approach and a suitable correction technique was a good choice. Not only were the results realistic, the simulations were exceptionally fast and could be performed within a few hours on a conventional computer. The 2D method is therefore well suited for performing parameter studies to further analyze different aspects related to the fan broadband noise mechanism. However, it should be noted that some effects like acoustic cut-on effects tend to be exaggerated for 2D simulations compared to 3D simulations. In contrast to the 2D method, the 3D method is more expensive and its simulation setup requires more user effort. Firstly, 3D simulations require a finer and more high-quality mesh design. Secondly, these simulations are more prone to numerical instabilities, in particular where CAA boundary conditions at the duct walls interact with fRPM patches. Compared to other measures, the introduction of local damping spots near the duct walls is less intrusive. Nonetheless, they can have an effect, especially for simulations featuring a reduced, radial domain. While the 2D approach is well suited for the investigated fan, the 3D fRPM-fan

approach is necessary when considering more complex geometrical features such as leading edge serrations or when studying the impact of anisotropic turbulence.

Acknowledgments

Funding: The presented ACAT1 data were obtained in the frame of the project TurboNoiseBB, which has received funding from the European Union's
 805 Horizon 2020 research and innovation program under grant agreement No. 690714.

The authors also thank Roland Ewert, Jürgen Dierke, and Nils Reiche (DLR) for their continued support and advice.

810 Appendix A. Influence of constant versus radially varying turbulence characteristics

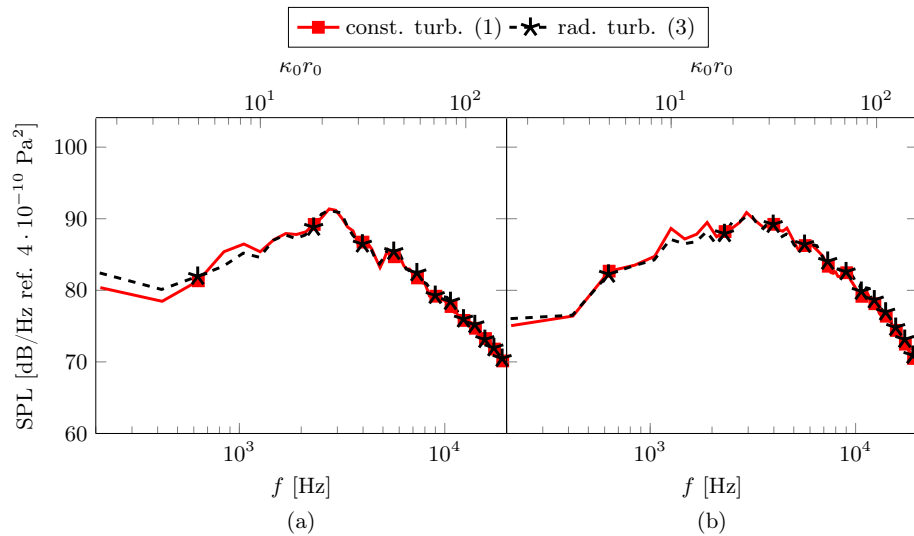


Figure A.17: Influence of constant versus radially varying turbulence characteristics on sound pressure level spectra (a) up- and (b) downstream of the stator row.

The 3D simulations used for direct comparisons with 2D simulations were performed with constant turbulence characteristics, which were determined by

radially averaging transverse velocity frequency spectra and fitting the result
 815 with a von Kármán spectrum to determine the turbulent kinetic energy and
 the turbulent length scale. This choice is convenient as it simplifies the di-
 rect comparison. To ensure that this approach, which is in accordance with
 the 3D-equivalent method, is reasonable, two simulations were performed (see
 Fig. A.17). The sound pressure spectra up- and downstream of the stator row
 820 are indeed nearly identical.

Appendix B. Influence of local damping at the duct walls of 3D sim- ulations

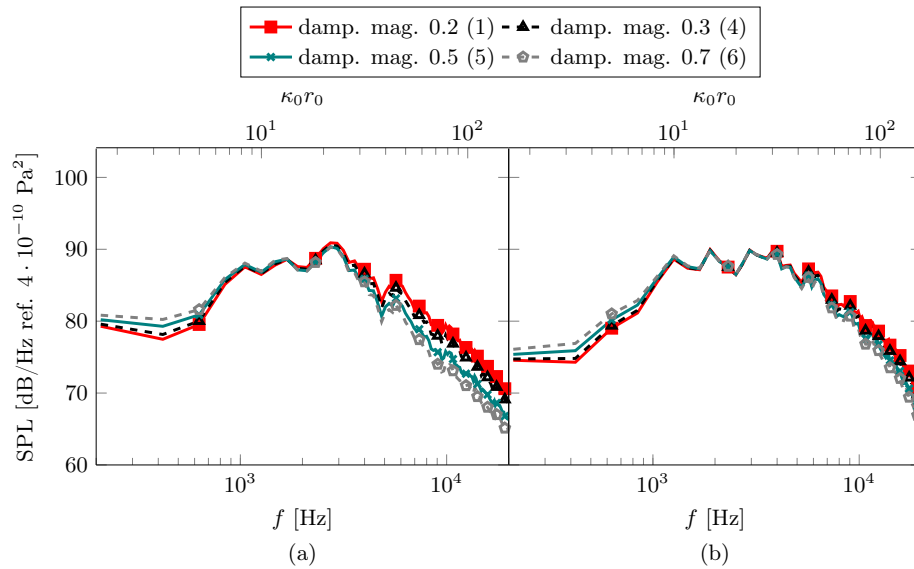


Figure B.18: Influence of local damping at duct walls on sound pressure level spectra (a) up- and (b) downstream of the stator row.

Local damping spots featuring a Gaussian shape and small radius were im-
 posed in certain sections of the duct walls to increase the numerical stability
 825 of 3D simulations. This measure is less invasive than increasing the global
 damping, which is often done as it is more convenient and easier to realize.
 Nonetheless, any kind of damping can have an impact. Therefore, several sim-

ulations featuring different relative damping magnitudes ranging between 0.2 and 0.7 were performed. A further reduction of the relative damping magnitude leads to numerical instabilities in areas of the mesh close to the vortex source patch or in regions featuring flow gradient. The impact of the relative damping magnitude can be seen in Fig. B.18. Note that the spectra are shown after the same sampling time. Figure B.18 shows that the sound pressure levels are least impacted in the mid frequency range, which includes the critical peak of the spectrum. In the low frequency regime, reducing the damping magnitude leads to lower levels. Conversely, sound pressure levels increase with decreasing damping magnitudes at high frequencies. The effect also is less pronounced downstream of the stator vanes than upstream of the stator vanes. This is likely a consequence of the fact that most flow domains prone to instabilities are located upstream of the stator. In conclusion, the local damping does play a role, therefore the magnitude for all 3D simulations was reduced to the lowest possible level that still permits numerically stable solutions. It is also conjectured that this effect is more pronounced for the reduced radial domain because the relative domain covered by local damping spots is larger than for the full domain.

Appendix C. Influence of reducing simulation domains in radial and circumferential direction

To reduce computational effort and enable comprehensive parameter studies, the computational domain was restricted to 11 stator vanes and the radial domain was reduced for 3D simulations.

Reducing the radial domain seems to have a small impact at most frequencies as shown in Fig. C.19. At higher frequencies, the sound pressure levels are higher for the simulations featuring a full stator domain than for the simulation featuring a reduced radial domain. This may not be directly related to the difference in span but could be an artifact of the local damping spots, which were discussed in the preceding section. While the lowest, relative damping

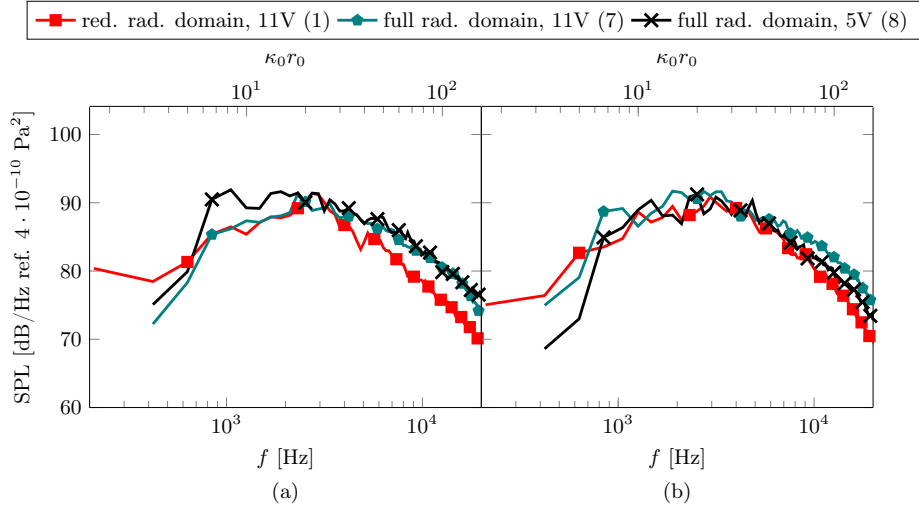


Figure C.19: Influence of reductions of the 3D simulation domain on sound pressure level spectra (a) up- and (b) downstream of the stator row.

magnitude is set at a higher value for the full domain simulations due to stability limitations, the number of damping spots pro unit volume is lower.

According to analytical formulations for in-duct fan broadband noise as e. g. described by Guérin et al. [35], one can formulate the following proportionality for the acoustic pressure p' :

$$p'^2 \propto \frac{V}{R^2} r, \quad (\text{C.1})$$

where V denotes the number of stator vanes, r is some radial position of the source, and R is the tip radius. The fraction $\frac{1}{R^2}$ is related to the in-duct Green's function. It can be assumed that $r \approx R$, which is exactly true for 2D simulations. A reduction of the number of stator vanes essentially reduces the duct radius r due to the imposed periodic boundary conditions in the circumferential direction. Therefore, the duct radius can be expressed as follows:

$$r = \frac{Vs_V}{2\pi}, \quad (\text{C.2})$$

where s_V describes the stator pitch, which is a constant in 2D space. Thus, the sound pressure level is proportional to a constant $p'^2 \propto \frac{2\pi}{s_V}$ and it can thus be expected that the sound pressure level is independent of the number of stator

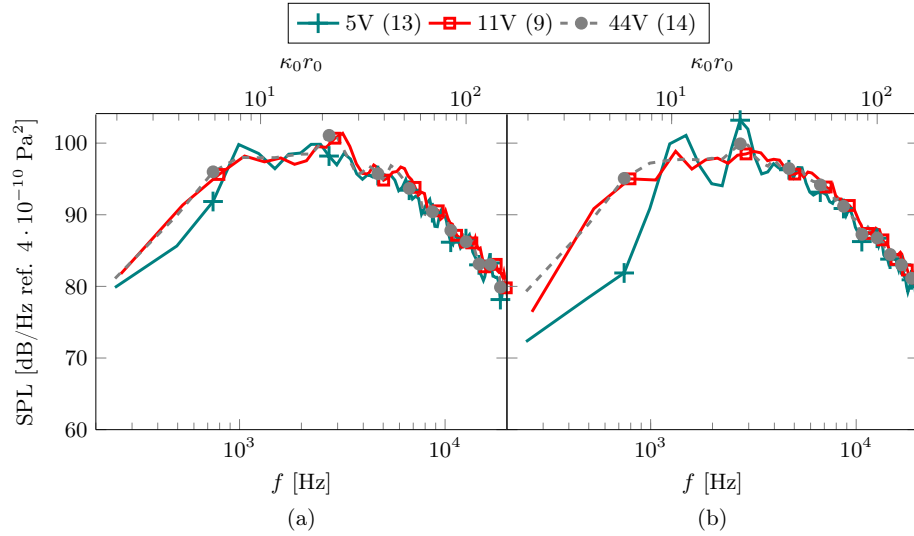


Figure C.20: Influence of a circumferential reduction of the 2D simulation domain on sound pressure level spectra (a) up- and (b) downstream of the stator row

vanes, i. e. a reduction of the circumferential domain. In fact, Fig. C.20 shows that the solutions of all 2D simulations agree well at high frequencies, while larger deviations - particularly for the simulation containing only 5 stator vanes - can be seen at lower frequencies. The peaks at low frequencies for simulation 13 are related to acoustic modes, which transition from cut-off to cut-on at certain frequencies. Since the cut-on frequency of modes is inversely proportional to the duct circumference, more modes are cut-on for an increasing duct radius, which explains why these effects are less relevant for simulations featuring a higher number of stator vanes. It also means that more modes are cut-on at higher frequencies, which lessens the impact of each additional, cut-on mode. Similar observations were also made in other works [10, 13, 14]. The simulation containing all 44 stator vanes has the smoothest spectra but is overall very similar to the simulation including only 11 stator vanes. It can therefore be concluded that the reduction to 11 stator vanes is a reasonable choice. It is interesting to note that these cut-on effects do not seem to play a significant role for 3D simulations. For 2D simulations, the cut-on frequency is related to

one specific frequency due to its reduction to one specific duct radius. As a 3D simulation spans a range of radii, these cut-on effects are smeared and likely
 880 much less distinct as a consequence.

Appendix D. Supercritical turbulence gusts of a von Kármán turbulence

Von Kármán turbulence describes homogeneous, isotropic turbulence and is a popular assumption for turbomachinery applications as its spectral shape
 885 resembles measured spectra. For completeness, some useful formulas and definitions for von Kármán turbulence are given in this section. The energy of the von Kármán spectrum in terms of the three-dimensional wavenumber space is given as:

$$E(|\mathbf{k}|) = \frac{55}{9\pi} u'^2 \Lambda \frac{|\hat{\mathbf{k}}|^4}{(1 + |\hat{\mathbf{k}}|^2)^{17/6}}, \quad (\text{D.1})$$

where the bold variables indicate vector quantities. The wavenumber vector is
 890 defined in terms of the direction of the mean velocity and has a components in streamwise (1), transverse (2), and radial (3) dimensions: $\mathbf{k} = (k_1, k_2, k_3)^T$. The wavenumber is often normalized with $k_e = \frac{\sqrt{\pi}\Gamma(5/6)}{\Lambda\Gamma(1/3)}$, hence $\hat{\mathbf{k}} = \mathbf{k}/k_e$. The integral turbulent length scale is indicated by Λ , whereas u'^2 is related to the turbulent kinetic energy $k = \frac{3}{2}u'^2$ under the assumption of isotropy.

The transverse velocity component is the most critical for fan broadband noise. Its spectrum can be related to the energy spectrum as follows:

$$\Phi_{22}(k_1, k_2, k_3) = \frac{E(\mathbf{k})}{4\pi|\mathbf{k}|^2} \left(1 - \frac{k_2^2}{|\mathbf{k}|^2}\right). \quad (\text{D.2})$$

This three-dimensional spectrum can be integrated over the transverse wavenumber component from negative to positive infinity to compute a two-dimensional transverse velocity spectrum:

$$\Phi_{22}(k_1, k_3) = \frac{4u'^2}{9\pi k_e^2} \frac{\hat{k}_1^2 + \hat{k}_3^2}{(1 + \hat{k}_1^2 + \hat{k}_3^2)^{7/3}}. \quad (\text{D.3})$$

The one-dimensional transverse velocity spectrum in terms of the streamwise wavenumber k_1 can be derived by integrating over k_3 from negative to positive infinity:

$$\Phi_{22}(k_1) = \frac{u'^2 \Lambda}{2\pi} \frac{1 + \frac{8}{3} \hat{k}_1^2}{(1 + \hat{k}_1^2)^{11/6}}. \quad (\text{D.4})$$

For two-dimensional turbulence, the transverse velocity spectrum differs and can be derived according to Pope [57]:

$$\Phi_{22}^{2D}(k_1) = -k_1 \frac{d\Phi_{11}(k_1)}{dk_1}, \quad (\text{D.5})$$

where the streamwise velocity spectrum $\Phi_{11}(k_1)$ is identical for 2D and 3D turbulence and is equal to:

$$\Phi_{11}(k_1) = \frac{u'^2 \Lambda}{\pi} \frac{1}{(1 + \hat{k}_1^2)^{5/6}}. \quad (\text{D.6})$$

Solving Eq. D.5 using the definition in Eq. D.6 results in a 2D, transverse velocity spectrum:

$$\Phi_{22}^{2D}(k_1) = \frac{5u'^2 \Lambda}{3\pi} \frac{\hat{k}_1^2}{(1 + \hat{k}_1^2)^{11/6}}. \quad (\text{D.7})$$

Eq. D.3 can also be integrated to only include supercritical modes according to Graham [21]:

$$2 \int_0^{\frac{\kappa_0}{\beta} (1 - \frac{M|\tan(\gamma)|}{\beta})} \Phi_{22}(k_1, k_3) dk_3 = \quad (\text{D.8})$$

$$2 \frac{4u'^2}{9\pi k_e^2} \left[I \left(k_1, k_3 = \frac{\kappa_0}{\beta} \left(\frac{\beta - M|\tan(\gamma)|}{\beta} \right) \right) - I(k_1, k_3 = 0) \right].$$

The definite integral I can be expressed as follows:

$$I(k_1, k_3) = \left(\hat{k}_3 \left(-(1 + \hat{k}_1^2)^2 (3 + 8\hat{k}_1^2) \left(\frac{1 + \hat{k}_1^2 + \hat{k}_3^2}{1 + \hat{k}_1^2} \right)^{4/3} {}_2F_1 \left(\frac{1}{3}, \frac{1}{2}, \frac{3}{2}, -\frac{\hat{k}_3^2}{1 + \hat{k}_1^2} \right) \right. \right. \\ \left. \left. + 24\hat{k}_1^4 + 3\hat{k}_1^2 (9 + 8\hat{k}_3^2) + 9\hat{k}_3^2 + 3 \right) \right) / \left(16 (1 + \hat{k}_1^2)^2 (1 + \hat{k}_1^2 + \hat{k}_3^2)^{4/3} \right). \quad (\text{D.9})$$

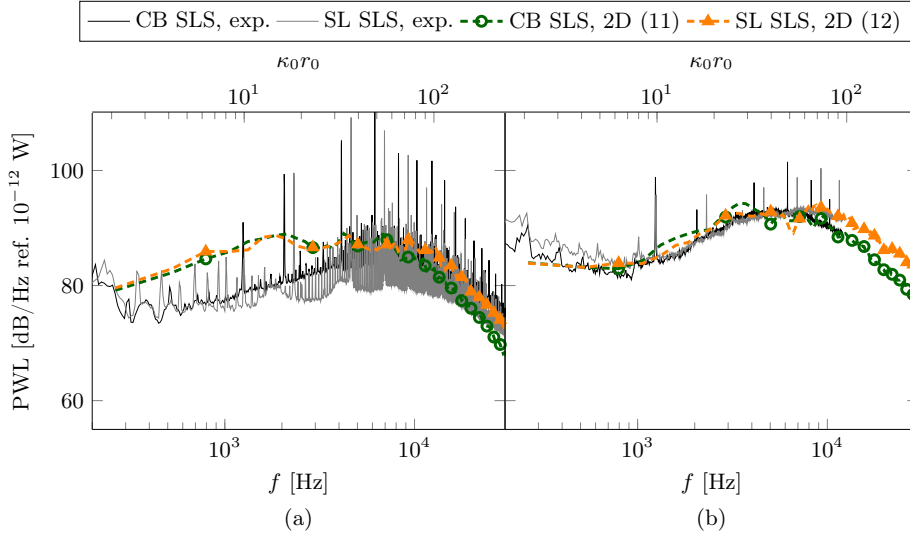


Figure E.21: Comparison of experimental and numerical sound power levels (a) up- and (b) downstream of the stator vanes for operating points CB SLS and SL SLS.

895 Appendix E. Comparison of numerical and experimental data at high-speed operating points

Experimental and 2D, numerical sound power level spectra up- and downstream of the stator row are shown in Fig. E.21. Note that the shown numerical values do not contain any corrections, which means that the numerical results are expected to be too high and the good agreement of the downstream spectra is therefore misleading. For the upstream spectra, the numerical spectra do not include any rotor blockage effects, which are expected to be more relevant at high speeds as discussed by Blázquez and Corral [12].

The numerical and experimental trends of operating points CB SLS and SL SLS with respect to the operating point AP SLS are shown in Figures E.22 and E.23. As for the operating point AP LN, the tendency of the Delta curves is well captured.

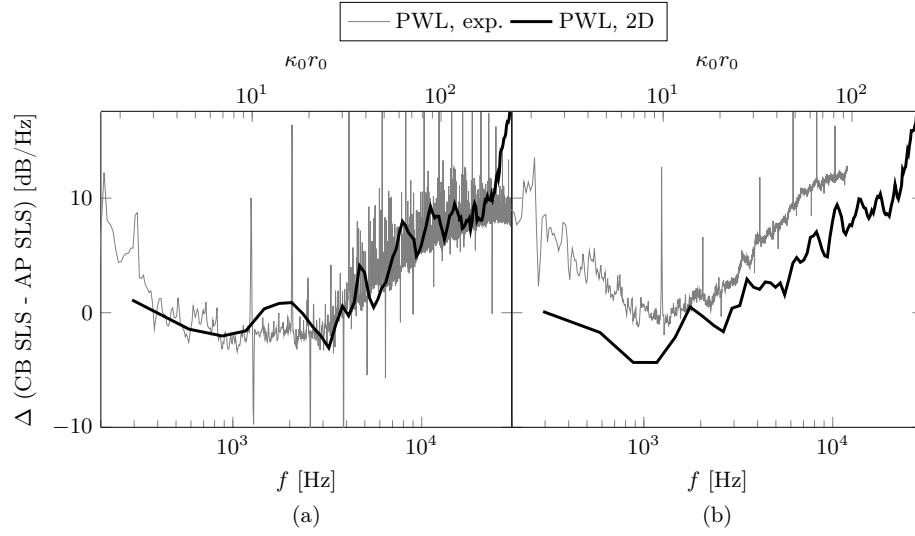


Figure E.22: Comparison of numerical and experimental trends (a) up- and (b) downstream of the stator vanes for the operating point CB SLS.

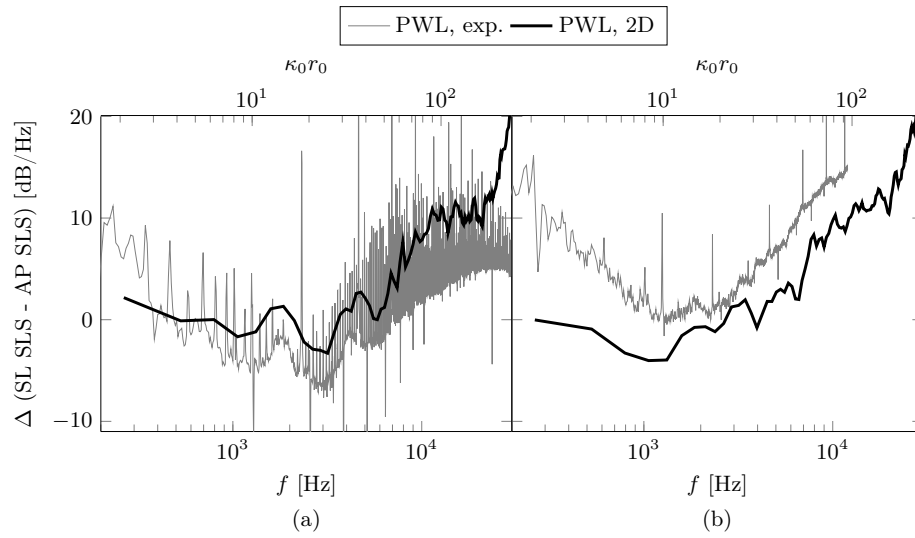


Figure E.23: Comparison of numerical and experimental trends (a) up- and (b) downstream of the stator vanes for the operating point SL SLS.

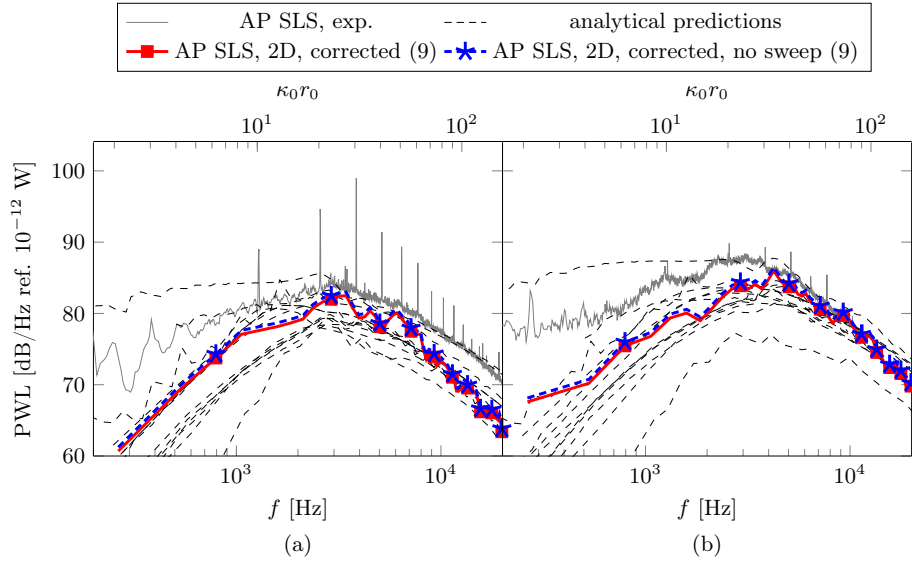


Figure F.24: Comparison of corrected, 2D results to experimental and analytical [35] sound power levels (a) up- and (b) downstream of the stator vanes for operating point AP SLS.

Appendix F. Comparison of corrected, 2D results to experimental and analytical data

910 In Figures F.24, F.25, and F.26, the corrected, 2D results are compared to experimental as well as analytical predictions using different models, which were initially presented and discussed by Guérin et al. [35]. As observed for the 3D results, the corrected, 2D results are within a similar range as the analytical predictions. This indicates that the results and the correction technique are reasonable. Numerical, downstream sound power levels underestimate experimental levels. Numerically predicted upstream sound power levels in comparison to measurements increase relative to the rotational speed, which can likely be explained by rotor blockage effects.

915

References

- 920 [1] R. Jaron, Aeroakustische Auslegung von Triebwerksfans mittels multidisziplinärer Optimierungen (Aeroacoustic design of engine fans using multidis-

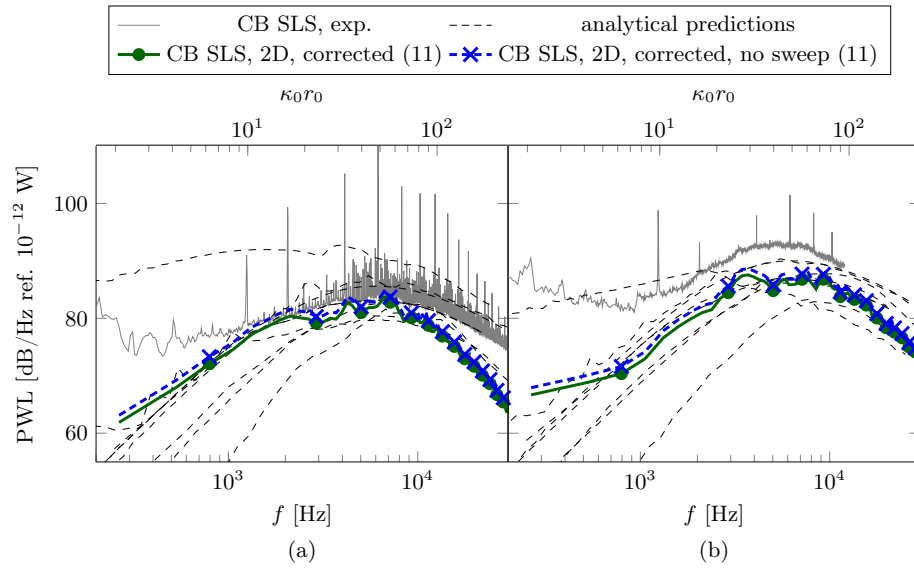


Figure F.25: Comparison of corrected, 2D results to experimental and analytical [35] sound power levels (a) up- and (b) downstream of the stator vanes for operating point CB SLS.

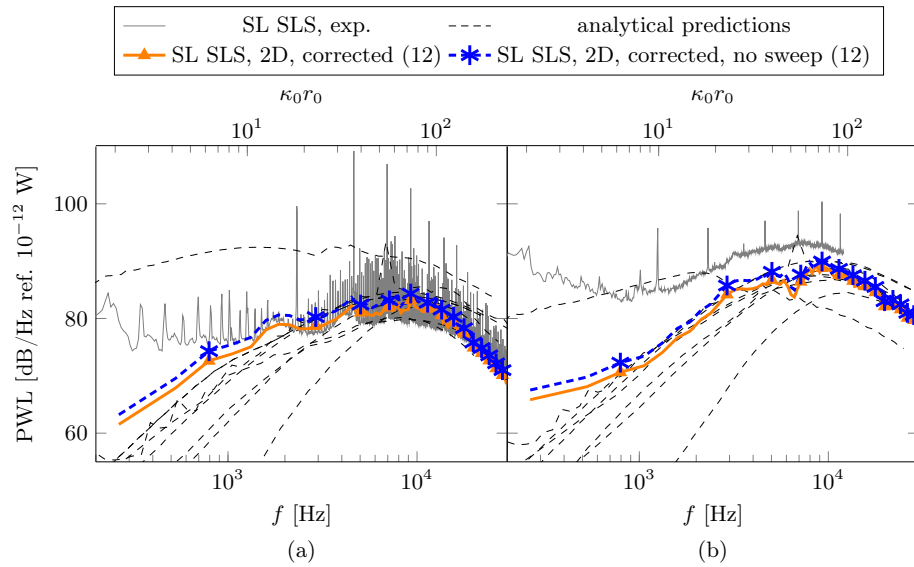


Figure F.26: Comparison of corrected, 2D results to experimental and analytical [35] sound power levels (a) up- and (b) downstream of the stator vanes for operating point SL SLS.

ciplinary optimizations), Doctoral thesis, TU Berlin, Berlin (2018).

URL <https://doi.org/10.14279/depositonce-7057>

[2] A. Careta, F. Sagués, J. M. Sancho, Stochastic generation of homogeneous
925 isotropic turbulence with well-defined spectra, *Physical Review E* 48 (3)
(1993) 2279–2287 (1993).

URL <https://doi.org/10.1103/PhysRevE.48.2279>

[3] R. Ewert, Broadband slat noise prediction based on CAA and stochastic
sound sources from a fast random particle-mesh (RPM) method, *Comput-
930 ers & Fluids* 37 (4) (2008) 369–387 (2008).

URL <https://doi.org/j.compfluid.2007.02.003>

[4] R. H. Kraichnan, Diffusion by a random velocity field, *Physics of Fluids*
(1958-1988) 13 (1) (1970) 22–31 (1970).

URL <https://doi.org/10.1063/1.1692799>

[5] W. Bechara, C. Bailly, P. Lafon, S. M. Candel, Stochastic approach to
935 noise modeling for free turbulent flows, *AIAA Journal* 32 (3) (1994) 455–
463 (1994).

URL <https://doi.org/10.2514/3.12008>

[6] M. Billson, L.-E. Eriksson, L. Davidson, Jet noise prediction using stochas-
940 tic turbulence modeling, in: 9th AIAA/CEAS Aeroacoustics Conference,
Hilton Head, South Carolina, USA, 2003 (2003).

URL <https://doi.org/10.2514/6.2003-3282>

[7] N. Jarrin, S. Benhamadouche, D. Laurence, R. Prosser, A synthetic-eddy-
method for generating inflow conditions for large-eddy simulations, *Inter-
945 national Journal of Heat and Fluid Flow* 27 (4) (2006) 585–593 (Aug. 2006).

URL <https://doi.org/10.1016/j.ijheatfluidflow.2006.02.006>

[8] A. Sescu, R. Hixon, Toward low-noise synthetic turbulent inflow conditions
for aeroacoustic calculations, *International Journal for Numerical Methods*

- in Fluids 73 (12) (2013) 1001–1010 (2013).
950 URL <https://doi.org/10.1002/flid.3833>
- [9] J. W. Kim, S. Haeri, An advanced synthetic eddy method for the computation of aerofoil-turbulence interaction noise, *Journal of Computational Physics* 287 (2015) 1–17 (2015).
URL <https://doi.org/10.1016/j.jcp.2015.01.039>
- 955 [10] A. Wohlbrandt, C. Kissner, S. Guérin, Impact of cyclostationarity on fan broadband noise prediction, *Journal of Sound and Vibration* 420 (2018) 142–164 (Apr. 2018).
URL <https://doi.org/10.1016/j.jsv.2018.01.039>
- [11] C. A. Kissner, S. Guérin, Influence of Wake and Background Turbulence
960 on Predicted Fan Broadband Noise, *AIAA Journal* 58 (2) (2019) 659–672 (2019).
URL <https://doi.org/10.2514/1.J058148>
- [12] R. Blázquez-Navarro, R. Corral, Prediction of fan acoustic blockage on fan/outlet guide vane broadband interaction noise using frequency domain
965 linearised navier–stokes solvers, *Journal of Sound and Vibration* 500 (2021) 116033 (2021).
URL <https://doi.org/10.1016/j.jsv.2021.116033>
- [13] F. Gea-Aguilera, Aerodynamic and Aeroacoustic Modelling of Engine Fan Broadband Noise, PhD thesis, University of Southampton (2017).
970 URL <https://eprints.soton.ac.uk/412640/>
- [14] C. A. Kissner, S. Guérin, M. Behn, Assessment of a 2D Synthetic Turbulence Method for Predicting the ACAT1 Fan’s Broadband Noise, in: 25th AIAA/CEAS Aeroacoustics Conference, 2019 (2019).
URL <https://doi.org/10.2514/6.2019-2501>
- 975 [15] R. K. Amiet, Acoustic radiation from an airfoil in a turbulent stream,

Journal of Sound and Vibration 41 (4) (1975) 407–420 (Aug. 1975).

URL [https://doi.org/10.1016/S0022-460X\(75\)80105-2](https://doi.org/10.1016/S0022-460X(75)80105-2)

- [16] M. Dieste, Random-vortex-particle methods applied to broadband fan interaction noise, Ph.D. thesis, University of Southampton (2011).

980 URL <http://eprints.soton.ac.uk/id/eprint/192591>

- [17] T. Hainaut, G. Gabard, V. Clair, CAA Study of Airfoil Broadband Interaction Noise Using Stochastic Turbulent Vorticity Sources, in: 21st AIAA/CEAS Aeroacoustics Conference, American Institute of Aeronautics and Astronautics, 2015 (2015).

985 URL <https://doi.org/10.2514/6.2015-2222>

- [18] F. Gea-Aguilera, J. Gill, X. Zhang, Synthetic turbulence methods for computational aeroacoustic simulations of leading edge noise, Computers & Fluids 157 (2017) 240–252 (2017).

URL <https://doi.org/10.1016/j.compfluid.2017.08.039>

- 990 [19] R. Ewert, C. Appel, J. Dierke, M. Herr, RANS/CAA based prediction of NACA 0012 broadband trailing edge noise and experimental validation, in: 15th AIAA/CEAS Aeroacoustics Conference, Miami, Florida, USA, 2009 (2009).

URL <https://doi.org/10.2514/6.2009-3269>

- 995 [20] C. Polacsek, V. Clair, G. Reboul, H. Deniau, Turbulence-airfoil interaction noise reduction using wavy leading edge: an experimental and numerical study, in: 40th International Congress and Exposition on Noise Control Engineering 2011 (INTER-NOISE 2011), Osaka, Japan, 2011 (2011).

URL <https://hal.archives-ouvertes.fr/hal-02086677>

- 1000 [21] J. M. R. Graham, Similarity rules for thin aerofoils in non-stationary subsonic flows, Journal of Fluid Mechanics 43 (4) (1970) 753–766 (1970).

URL <https://doi.org/10.1017/S0022112070002719>

- [22] S. A. Glegg, The response of a swept blade row to a three-dimensional gust, *Journal of Sound and Vibration* 227 (1) (1999) 29–64 (1999).
1005 URL <https://doi.org/10.1006/jsvi.1999.2327>
- [23] C. Kissner, S. Guérin, Fan Broadband Noise Prediction for the ACAT1 Fan Using a Three-Dimensional Random Particle Mesh Method, in: 26th AIAA/CEAS Aeroacoustics Conference, 2020 (2020).
URL <https://doi.org/10.2514/6.2020-2520>
- 1010 [24] A. Wohlbrandt, Stochastische Verfahren zur Simulation von Breitband-schall in Triebwerksfans (Stochastic method for simulating broadband noise of engine fans), Doctoral thesis, TU Berlin, Berlin (2017).
URL <https://doi.org/10.14279/depositonce-6533>
- [25] M. Siefert, R. Ewert, Sweeping Sound Generation in Jets Realized with
1015 a Random Particle-Mesh Method, in: 15th AIAA/CEAS Aeroacoustics Conference, Miami, Florida, USA, 2009 (2009).
URL <https://doi.org/10.2514/6.2009-3369>
- [26] R. J. Purser, W.-S. Wu, D. F. Parrish, N. M. Roberts, Numerical aspects
1020 of the application of recursive filters to variational statistical analysis. Part II: Spatially inhomogeneous and anisotropic general covariances, *Monthly Weather Review* 131 (8) (2003) 1536–1548 (2003).
URL <https://doi.org/10.1175//2543.1>
- [27] A. Wohlbrandt, N. Hu, S. Guérin, R. Ewert, Analytical reconstruction of
1025 isotropic turbulence spectra based on the gaussian transform, *Computers and Fluids* 132 (2016) 46–50 (2016).
URL <https://doi.org/10.1016/j.compfluid.2016.03.023>
- [28] J. W. Delfs, M. Bauer, R. Ewert, H. Grogger, M. Lummer, T. Lauke, Nu-
1030 merical Simulation of Aerodynamic Noise with DLR’s aeroacoustic code PIANO, Tech. rep., German Aerospace Center (DLR), Braunschweig, Germany (2008).
URL <https://elib.dlr.de/118928/>

- [29] L. N. Long, A nonconservative nonlinear flowfield splitting method for 3-D unsteady fluid dynamics, in: 6th AIAA/CEAS Aeroacoustics Conference, Maui, Hawaii, USA, 2000 (2000).
1035 URL <https://doi.org/10.2514/6.2000-1998>
- [30] C. A. Kissner, A. M. Wohlbrandt, S. Guérin, Enhanced Fan Broadband Noise Prediction Based on a 2d Synthetic Turbulence Method, in: 24th AIAA/CEAS Aeroacoustics Conference, Atlanta, Georgia, USA, 2018 (2018).
1040 URL <https://doi.org/10.2514/6.2018-3452>
- [31] F. Q. Hu, M. Y. Hussaini, J. L. Manthey, Low-dissipation and low-dispersion Runge - Kutta schemes for computational acoustics, Journal of Computational Physics 124 (1) (1996) 177–191 (1996).
URL <https://doi.org/10.1006/jcph.1996.0052>
- 1045 [32] C. K. Tam, J. C. Webb, Dispersion-relation-preserving finite difference schemes for computational acoustics, Journal of Computational Physics 107 (2) (1993) 262–281 (1993).
URL <https://doi.org/10.1006/jcph.1993.1142>
- [33] R. Ewert, J. Dierke, A. Neifeld, S. A. Moghadam, Linear-and Non-Linear
1050 Perturbation Equations with Relaxation Source Terms for Forced Eddy Simulation of Aeroacoustic Sound Generation, in: 20th AIAA/CEAS Aeroacoustics Conference, Atlanta, Georgia, USA, 2014 (2014).
URL <https://doi.org/10.2514/6.2014-3053>
- [34] S. Guérin, C. A. Kissner, B. Kajasa, R. Jaron, M. Behn, B. Pardowitz,
1055 U. Tapken, S. Hakansson, R. Meyer, L. Enghardt, Noise prediction of the ACAT1 fan with a RANS-informed analytical method: success and challenge, in: 25th AIAA/CEAS Aeroacoustics Conference, 2019 (2019).
URL <https://doi.org/10.2514/6.2019-2500>
- [35] S. Guérin, C. Kissner, P. Seeler, R. Blázquez, P. Carrasco Laraña,
1060 H. de Laborderie, D. Lewis, P. Chaitanya, C. Polacsek, J. Thisse, ACAT1

Benchmark of RANS-Informed Analytical Methods for Fan Broadband Noise Prediction: Part II—Influence of the Acoustic Models, *Acoustics* 2 (3) (2020) 617–649 (2020).

URL <https://doi.org/10.3390/acoustics2030033>

- 1065 [36] C. Kissner, S. Guérin, P. Seeler, M. Billson, P. Chaitanya, P. Carrasco Laraña, H. de Laborderie, B. François, K. Lefarth, D. Lewis, G. Montero Villar, T. Nodé-Langlois, ACAT1 Benchmark of RANS-Informed Analytical Methods for Fan Broadband Noise Prediction—Part I—Influence of the RANS Simulation, *Acoustics* 2 (3) (2020) 539–578 (2020).

1070 URL <https://doi.org/10.3390/acoustics2030029>

- [37] R. Meyer, S. Hakansson, W. Hage, L. Enghardt, Instantaneous flow field measurements in the interstage section between a fan and the outlet guiding vanes at different axial positions, in: *13th European Conference on Turbomachinery Fluid Dynamics and Thermodynamics*, 2019 (2019).

1075 URL <https://elib.dlr.de/133297/>

- [38] U. Tapken, M. Behn, M. Spitalny, B. Pardowitz, Radial mode breakdown of the ACAT1 fan broadband noise generation in the bypass duct using a sparse sensor array, in: *25th AIAA/CEAS Aeroacoustics Conference*, 2019 (2019).

1080 URL <https://doi.org/10.2514/6.2019-2525>

- [39] A. Pereira, M. Jacob, Experimental assessment of in-duct modal content of fan broadband noise via iterative bayesian inverse approach, in: *Proceedings of the Berlin Beamforming Conference*, Berlin, Germany, 2020, pp. 2–3 (2020).

1085 URL <http://www.bebec.eu/Downloads/BeBeC2020/Papers/BeBeC-2020-D20.pdf>

- [40] K. Becker, K. Heitkamp, E. Kügeler, Recent Progress in a Hybrid Grid CFD Solver for Turbomachinery Flows, in: *Proc.V European Conference*

- on Computational Fluid Dynamics ECCOMAS CFD 2010, 2010 (2010).
1090 URL <https://elib.dlr.de/68938/>
- [41] R.-D. Cécora, R. Radespiel, B. Eisfeld, A. Probst, Differential Reynolds-stress modeling for aeronautics, *AIAA Journal* 53 (3) (2015) 739–755 (2015).
URL <https://doi.org/10.2514/1.J053250>
- 1095 [42] F. R. Menter, Two-equation eddy-viscosity turbulence models for engineering applications, *AIAA Journal* 32 (8) (1994) 1598–1605 (1994).
URL <https://doi.org/10.2514/3.12149>
- [43] J. D. Denton, U. K. Singh, Time marching methods for turbomachinery flow calculation, in: *In Von Karman Inst. for Fluid Dyn. Appl. of Numerical Methods to Flow Calculations in Turbomachines*, 1979 (1979).
1100 URL <https://ui.adsabs.harvard.edu/abs/1979anmf.vkif.....D/abstract>
- [44] C. Polacsek, A. Cader, M. Buszyk, R. Barrier, F. Gea-Aguilera, H. Posson, Aeroacoustic design and broadband noise predictions of a fan stage with serrated outlet guide vanes, *Physics of Fluids* 32 (10) (2020) 1–20 (2020).
1105 URL <https://doi.org/10.1063/5.0020190>
- [45] Moreau, Antoine, A unified analytical approach for the acoustic conceptual design of fans of modern aero-engines, Ph.D. thesis, TU Berlin (2017).
URL <https://doi.org/10.14279/depositonce-5935>
- 1110 [46] J. Gill, X. Zhang, P. Joseph, T. Nodé-Langlois, Reduced dimension modeling of leading edge turbulent interaction noise, in: *20th AIAA/CEAS Aeroacoustics Conference*, Atlanta, Georgia, USA, 2014 (2014).
URL <https://doi.org/10.2514/6.2014-2321>
- [47] C. L. Morfey, Sound transmission and generation in ducts with flow, *Journal of Sound and Vibration* 14 (1) (1971) 37–55 (1971).
1115 URL [https://doi.org/10.1016/0022-460X\(71\)90506-2](https://doi.org/10.1016/0022-460X(71)90506-2)

- [48] W. De Roeck, W. Desmet, M. Baelmans, P. Sas, An overview of high-order finite difference schemes for computational aeroacoustics, in: Proceedings of the International Conference on Noise and Vibration Engineering, 2004, pp. 353–368 (2004).
1120 URL <https://citeseerx.ist.psu.edu/viewdoc/download?doi=10.1.1.390.1563&rep=rep1&type=pdf>
- [49] U. Tapken, B. Pardowitz, M. Behn, Radial mode analysis of fan broadband noise, 23rd AIAA/CEAS Aeroacoustics Conference, 2017 (2017).
1125 URL <https://doi.org/10.2514/6.2017-3715>
- [50] M. Behn, B. Pardowitz, U. Tapken, Separation of tonal and broadband noise components by cyclostationary analysis of the modal sound field in a low-speed fan test rig, Fan2018, 2018 (2018).
URL <https://elib.dlr.de/126162/>
- [51] P. Joseph, C. L. Morfey, C. R. Lewis, Multi-mode sound transmission in ducts with flow, Journal of Sound and Vibration 264 (3) (2003) 523–544 (2003).
1130 URL [https://doi.org/10.1016/S0022-460X\(02\)01205-1](https://doi.org/10.1016/S0022-460X(02)01205-1)
- [52] M. Behn, U. Tapken, Investigation of Sound Generation and Transmission Effects Through the ACAT1 Fan Stage using Compressed Sensing-based Mode Analysis, in: 25th AIAA/CEAS Aeroacoustics Conference, Delft, Netherlands, 2019 (2019).
1135 URL <https://doi.org/10.2514/6.2019-2502>
- [53] D. Lewis, S. Moreau, M. C. Jacob, On the Use of RANS-informed Analytical Models to Perform Broadband Rotor-Stator Interaction Noise Predictions, in: 25th AIAA/CEAS Aeroacoustics Conference, 2019 (2019).
1140 URL <https://doi.org/10.2514/6.2019-2667>
- [54] A. Cader, C. Polacsek, T. L. Garrec, R. Barrier, F. Benjamin, M. C. Jacob, Numerical prediction of rotor-stator interaction noise using 3d CAA

- 1145 with synthetic turbulence injection, in: 24th AIAA/CEAS Aeroacoustics
Conference, 2018 (2018).
URL <https://doi.org/10.2514/6.2018-4190>
- [55] C. Polacsek, M. Daroukh, B. François, R. Barrier, Turbofan Broadband
Noise Predictions Based on a ZDES Calculation of a Fan-OGV Stage, in:
1150 Forum Acusticum, 2020 (2020).
URL <https://hal.archives-ouvertes.fr/hal-03181349/>
- [56] V. Clair, C. Polacsek, T. Le Garrec, G. Reboul, M. Gruber, P. Joseph, Ex-
perimental and numerical investigation of turbulence-airfoil noise reduction
using wavy edges, AIAA Journal 51 (11) (2013) 2695–2713 (2013).
1155 URL <https://doi.org/10.2514/1.J052394>
- [57] S. B. Pope, Turbulent Flows, IOP Publishing, 2001 (2001).
URL <https://doi.org/10.1088/0957-0233/12/11/705>